Second Harmonic Conversion Enhancement in 2-D Planar Photonic Crystals

by

Weiyang Jiang

B.Sc. Sichuan University, Chengdu, China, 1988

M.Sc. Tongji University, Shanghai, China, 1996

A THESIS SUBMITTED IN PARTIAL FULFILLMENT OF

THE REQUIREMENTS FOR THE DEGREE OF

MASTER OF SCIENCE

in

THE FACULTY OF GRADUATE STUDIES

DEPARTMENT OF PHYSICS AND ASTRONOMY

We accept this thesis as conforming

to the required standard

THE UNIVERSITY OF BRITISH COLUMBIA

October, 2002

In presenting this thesis in partial fulfillment of the requirements for an advanced degree at the University of British Columbia, I agree that the Library shall make it freely available for reference and study. I further agree that permission for extensive copying of this thesis for scholarly purposes may be granted by the head of my department or by his or her representatives. It is understood that copying or publication of this thesis for financial gain shall not be allowed without my written permission.

Department of physics
The University of British Columbia
Vancouver, Canada

Date October 11, 2002

Abstract

Two dimensional (2D) periodic texture in a thin GaAs semiconductor waveguide is used to dramatically enhance the second harmonic conversion efficiency of infrared laser radiation incident on the structure from above. A square lattice of through-holes was etched into a 140 nm thick layer of GaAs supported on a ~ 1μm thick alumina cladding layer. The pitch of 770 nm, and hole diameter of 320 nm, were chosen so that fundamental light at a wavelength of ~ 2μm could resonantly excite the lowest order band of leaky photonic eigenstates characteristic of the strongly textured membrane. The energy of the fundamental and second harmonic are both less than the band gap energy of the GaAs, thus avoiding any linear absorption. Used in this way, the structure acts effectively like a nonlinear cavity, where strong internal fields are generated in the GaAs waveguide core layer when the incident light excites a leaky photonic eigenstate. The 2^{nd} order polarization excited in the GaAs can also be resonant with photonic eigenstates at twice the fundamental frequency and in-plane wavevector.

Both model calculations and experimental results (obtained by J. Mondia at the University of Toronto) clearly demonstrate that the second harmonic conversion efficiency is dramatically influenced when the fundamental and/or the second harmonic fields are resonant with photonic bands. Peak enhancements of over 1000 times are observed under the "double-resonance" condition when both the fundamental and second harmonic fields excite photonic eigenstates, and the enhancement clearly tracks the in-coming and out-going dispersion of the photonic bands.

Contents

List of Figures

List of Tables

Acknowledgements

I would like to thank my supervisor Dr. Jeff F. Young for his continuous guidance and encouragement. He patiently provided me with clarifications and directions throughout my whole study. Without his enlightenment, it's impossible for me to finish this work and have a clearer vision on my further research.

I am also in debt to the members in Jeff Young's group for their discussions, suggestions, and assistance in my project. In particularly, I would like to thank: Dr. William Jody Mandeville for unreserved introduction of his experience on the whole e-beam processing; Allan Cowan for making me acquainted with the linear and non-linear code used in my thesis simulation; Mohammed Banaee for the many discussions we shared; Christina Kaiser for her enthusiastic help on the optics measurement, and on problems on computers equipments; Al Schmalz for his training me on SEM, ECR and always timely assistance on the problems I encountered on these equipments; Kuljit Virk for his clear explanation on his non-linear code; and expecially, Dr. Xiaonong Shen for her constructive discussion and resourceful help on the optical measurement.

In addition, I would like to sincerely thank my dear wife, Xuewei (Sherry), for her tremendous support throughout my study in UBC, and my daughter, Linda, for her understanding. Especially thanks to my parents-in-law, Yuwu and Fengyin, and my mother, Wenyin, for their support and helping me take care of my daughter, so that I could concentrate on the research work.

Chapter 1

Introduction

Photonic crystals are dielectric structures with a periodic refractive index. The spatial period of the refractive index modulation is called the lattice constant. In semiconductor materials, the lattice may introduce gaps into the energy band structure of the crystals, so that electrons are forbidden to propagate with certain frequencies in certain directions. If the lattice potential is strong enough, the gap might extend to all possible directions, resulting in a complete band gap. Photonic crystals do to photons what semiconductor crystals do to electrons. They create a situation in which photons are forbidden to propagate in certain directions. In general the periodicity of photonic crystals can be in one dimension (1D), two-dimensions (2D), or three dimensions (3D).

In 1987, Yablonovitch [11] and John [12] independently suggested, from different respects, that structures with periodic variations in dielectric constant could influence the nature of the modes in a material. Yablonovitch suggested that a three dimensional periodic array of dielectric scatterers possessing a complete band gap may lead to the inhibition of spontaneous emission, while John suggested that carefully prepared three dimensional photonic crystals with moderate disorder may result in strong Anderson localization of photons. In 1991, by drilling a dielectric block full of holes on the order of centimeters in diameter to form a face-centered cubic (FCC) crystal structure, Yablonovitch fabricated the first 3D periodic photonic crystal, which was supposed to posses a complete bandgap in the microwave regime [13]. Since then, many other 3D photonic crystal designs and experiments have appeared that offer complete photonic bandgaps, such as in a diamond structure [14], in highly symmetric photonic quasi-

crystals [15], in "layer-by-layer" photonic crystals [16,28], and in a 3D FCC polymer structure [29].

Compared with the difficulty of fabricating 3D photonic structures, 2D photonic crystal structures etched into semiconductor waveguides are relatively easy to fabricate and therefore are of substantial interest [17,23,24,25,26,27]. Although they cannot possess true optical band gaps, they do exhibit many of the attractive features of their 3D counterparts. Previous work in our lab has developed a linear model [1,2] for efficiently determining the specular reflectivity spectrum of two dimensionally textured slab waveguides. This model uses a Green's function technique to solve Maxwell equations. The results of this computer code have been validated by obtaining very good agreement between the simulation results and the experiment results obtained on square lattices and triangular lattices, with or without defects, etched into the planar GaAs waveguides [3,17].

Although most of the effort in the field has focused on the search for a material that exhibits a full photonic band gap, it has been recognized that nonlinear optical effects may play an important role in the development of more efficient opto-electronic devices, such as an intensity-driven optical limiter or an optical switch [18]. Optical frequency conversion by second order nonlinear interactions (via the second order susceptibility $\chi^{(2)}$) offers a way to obtain coherent light in various spectral regions. Second Harmonic Generation (SHG) is a two-photon process in which two photons are converted to a single photon. If the propagation wavevectors at the two frequencies satisfy $\vec{\beta}(2\omega) = 2\vec{\beta}(\omega)$ (this is called ideal phase-matching) quasi momentum is conserved and the interaction is allowed. In general, the linear dispersion of the crystal mismatches the phase between the different interacting optical waves. In a periodically modulated nonlinear material the conservation of momentum becomes the ''generalized phase

matching condition'' $\vec{\beta}(2\omega) = 2\vec{\beta}(\omega) + \vec{G}_i$, where $\vec{G}_i$ is one of the reciprocal-lattice vectors that describes the periodic modulation. The first example of a 2D periodic non-linear photonic crystal similar to that proposed by Berger [20] was experimentally realized by Broderick in bulk lithium niobate [21]. Internal conversion efficiencies of >80% were observed when the 2D reciprocal lattice vectors helped satisfy the GPM condition.

In our case, however, the 2D square lattice is textured not in a bulk material, but on a thin slab waveguide of GaAs, which has a thickness of 140 nm (less than half of the wavelength of the incident fundamental light and that of the second harmonic). While the GPM concept would apply directly to the second harmonic conversion process involving bound modes propagating in the plane of these textured waveguides, this thesis focuses on a qualitatively different mechanism for enhancing second harmonic conversion in periodically textured nonlinear media. It is shown below that when light incident on the surface of the textured waveguide excites leaky photonic eigenstates of the structure, the 2D-textured planar photonic crystal acts like a non-linear cavity. When both fundamental and second-harmonic polarizations excite leaky photonic bands, the second harmonic generation mechanism is not one of conversion versus distance in the direction of propagation, but one of an engineered enhancement of what is effectively surface second harmonic generation [22]. Uniform illumination from above can resonantly excite large local fields in the vicinity of the textured membrane, which in turn can be efficiently coupled back out in the form of an outward propagating plane wave in vacuum. It turns out that the overall external efficiency of this reflective harmonic conversion process has nothing directly to do with in plane propagation effects.

A nonlinear model was developed in our lab, to calculate the second harmonic [22,30] conversion efficiency for plane waves incident on 2D periodically textured nonlinear

waveguides. In this thesis, a 2D photonic crystal was designed by the author to achieve high second harmonic generation efficiency. A square lattice of though holes was etched into a 140 nm thick layer of GaAs waveguide supported on a ~ 1μm thick alumina cladding layer. The pitch of 770 nm, and hole diameter of 320 nm, were chosen so that fundamental light at a wavelength of ~ 2μm could resonantly excite the lowest order band of leaky photonic eigenstates characteristic of the strongly textured membrane. Used in this way, the structure acts effectively like a nonlinear cavity, where strong internal fields are generated in the GaAs waveguide core layer when the incident light excites a leaky photonic eigenstate. The 2^{nd} order polarization excited in the GaAs can also be resonant with photonic eigenstates at twice the fundamental frequency and in-plane wavevector. The energy of the second harmonic in this structure is less than the band gap energy of the GaAs in order to avoid complications due to absorption. Both model calculations done by the author, and experimental results obtained by J. Mondia at the University of Toronto, clearly demonstrate that the second harmonic conversion efficiency is dramatically influenced when the fundamental and/or the second harmonic fields are resonant with photonic bands.

The remainder of the thesis is organized as follows. In chapter 2, the band structures of untextured and square-lattice-textured slab waveguides are described. The linear and the non-linear models are briefly discussed, and the process by which the final sample was designed is described. Chapter 3 presents the procedure used to fabricate the designed sample. Chapter 4 presents the results of linear and non-linear light spectroscopy experiments on the textured planar waveguide described in chapter 3. The experimental data are compared with linear and non-linear simulations based on the Green's function formalism described in Chapter 2. Chapter 5 gives a discussion of the results, and the conclusions drawn from our work.

Chapter 2

Theory and Sample Design

This chapter briefly describes the electromagnetic properties of untextured and textured planar waveguides and summarizes the linear and nonlinear models developed by others in our group, but used extensively in this thesis to simulate the linear and second harmonic dispersion of GaAs waveguides textured with a 2D square lattice of through-holes. The latter part of the chapter describes how the structural parameters of the samples were designed to optimize the conditions for experimentally measuring second harmonic conversion via leaky modes in these structures.

2.1 Textured Planar Waveguides

The electromagnetic properties of untextured and textured waveguides are reviewed in sections 2.1.1 and section 2.1.2 respectively.

2.1.1 Untextured Planar Waveguides

The planar waveguides used in this work consist of a dielectric slab of high refractive index sandwiched by cladding layers with lower, and in general different refractive indices above and below. Light can be guided and confined in the high-index slab by total internal reflections at the core/cladding interfaces. In order to obtain a complete description of the modes of dielectric waveguides, Maxwell's equations must be solved separately for transverse electric (TE) and transverse magnetic (TM) polarized modes. TE (TM) polarized modes have their

electric (magnetic) field parallel to the layer interfaces (see section 2.3). A schematic dispersion diagram for an untextured, asymmetric slab waveguide (with air and a dielectric as the two different cladding layers) is shown in Fig. 2.1. The $\beta_{//}$ symbol refers to the in-plane wavevector of the harmonic solutions of the Maxwell equations in this planar geometry. The three straight lines represent the dispersion of light in homogeneous regions of air, core material, and cladding materials. The bold lines between the core light line and the cladding light line are the perfectly bound modes or slab modes that propagate without attenuation in the plane of the waveguide. The modes in this region undergo total internal reflections at the air-core and the core-cladding interfaces. The dark (grey) shaded areas represent a continuum of radiation modes. The modes in these regions can be thought as the plane waves incident from the air (cladding), reflected back from the core and cladding (air) layers, while not passing into the cladding (air) from the core due to total internal reflection. In general, there is no resonant enhancement of the fields in the core region of the guide in these shaded, continuum portions of the dispersion diagram. The area below the light line of the core material is a forbidden area, in which there are no electromagnetic modes that can propagate. There are an infinite number of discrete bound modes. Only the lowest two are shown here. The lowest bound mode is always TE polarized.

The planar waveguide used in the second harmonic experiments has an ~ 140nm thick core layer of GaAs (with n~ 3.3) supported on an ~1 μm thick cladding layer of wet-oxidized $Al_{0.98}Ga_{0.02}As$, which has a refractive index of ~ 1.6.

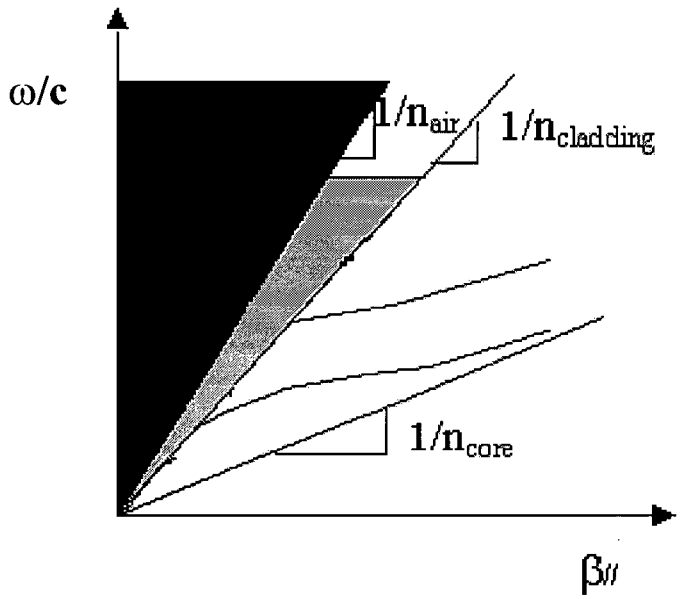

Figure 2.1: Schematic dispersion diagram for an untextured, asymmetric planar wave-guide (with air and a dielectric as the two different cladding layers). The bold lines are bound modes localized in the waveguide; the dark (grey) shaded areas represent the continuum of radiation modes. The three straight lines are the dispersion of light in air, in the core material, and in cladding materials.

2.1.2 Textured Planar Waveguides

A periodic structure textured on or in a planar waveguide presents a periodic scattering potential that modifies, or renormalizes, the slab-mode dispersion of photons described above [27] Bloch's theorem implies that all of the electromagnetic modes of the photonic crystal are of a Bloch form: that is they are the product of a periodic function having a period equal to that of the grating, times a phase factor $e^{i\vec{\beta}_{//}\bullet\vec{\rho}}$, where $\vec{\beta}_{//}$ is the in-plane wavevector of the mode, and $\vec{\rho}=\{x,y\}$. Just as in solid state physics, it is convenient to describe the excitation spectrum in terms of only the part of the reciprocal space spanned by the 1st Brillouin zone [33]. The dispersion diagram of a planar waveguide weakly textured with a 1D grating is shown

schematically in Fig. 2.2. In the diagram, $\vec{\beta}_g = 2\pi / \Lambda$ is the principal grating wavevector, and Λ is the lattice constant. The bands are zone-folded versions of the slab mode dispersion, renormalized by the scattering. Using this zone-folded scheme, some of the bound bands fall above the air light line, where they couple to radiation modes in the continuum. These remnants of the bound modes are referred to as resonant (leaky) modes, since they have Fourier components that radiate away from the core layer. Thus the "bound modes" in this type of structure are split into two distinct kinds. One set are truly bound (dotted and dashed curves) that exists below the light line of the cladding material, while the others are leaky modes (solid curves) that exists above the light line of the air (or more generally the cladding with the lowest refractive index). Band gaps open at the centre and edges of the 1st Brillouin zone because of the periodic potential. The higher the index-contrast is between the material of the grating layer and that of the cladding (air and alumina in our samples), the stronger the potential is, and therefore the bigger the band gaps are. The size of the gaps are also affected by the filling fraction of the grating.

Experimentally, we measured the reflection spectrum of broadband light in the specular direction. The broadband light incident at fixed angle corresponds to an angular cut through this dispersion diagram, as indicated by the dash-dotted line in Fig. 2.2. From the specular reflectivity spectrum, the resonant (leaky) modes can be detected and used to map out the dispersion diagram for the leaky modes.

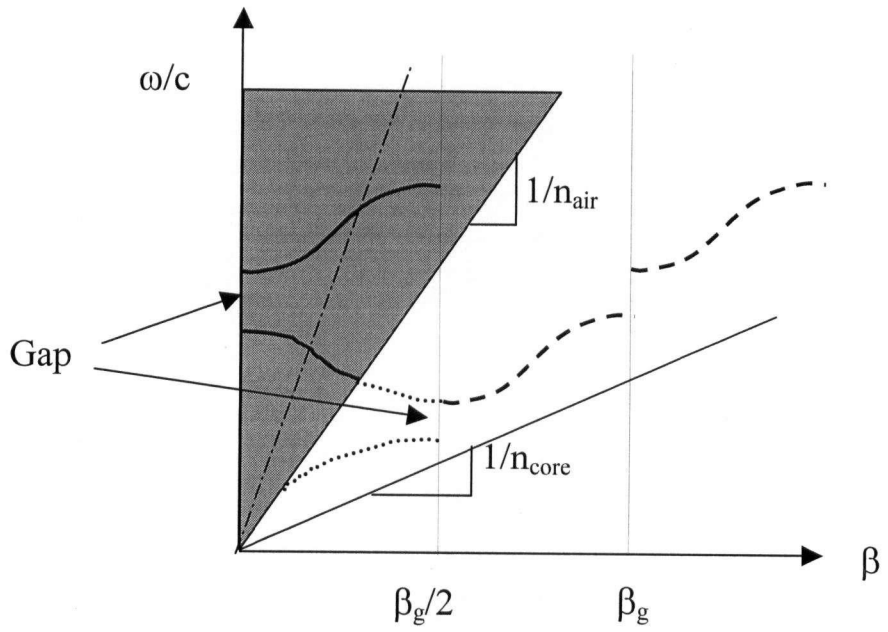

Figure 2.2: Schematic of the dispersion of electromagnetic modes in a 1D textured slab waveguide. The dashed lines are the dispersion curves in the extended zone scheme. The shaded area represents the continuum of radiation modes. The solid and solid-dotted lines are the dispersion curves of the bound modes in the folded-zone scheme. The dotted lines are truly bound modes and the solid lines are the resonant (leaky) modes. The Bragg condition ($\vec{\beta} = \vec{\beta}_g / 2$) is represented by the vertical dashed lines. The dash-dotted line represents the part of the bandstructure probed by a broadband source incident at a fixed angle.

2.2 Physical Interpretation of the Photonic Eigenstates

Figure 2.3 is a momentum space diagram that shows the nine dominant Fourier components of the dielectric scattering potential for a simple square lattice (solid dots). The corresponding 9 Fourier components of the induced electric field are included at $\vec{\beta} = \vec{\beta}_{inc} + i\beta_g \hat{x} + j\beta_g \hat{y}$ for $i, j = 0, \pm 1$, where $\vec{\beta}_{inc}$ is the in-plane wavevector of the plane wave assumed to be incident on the structure from the top halfspace. Figures 2.3(a) and 2.3(b) correspond to the incident wavevector, $\vec{\beta}_{inc}$, being aligned along the X symmetry direction and

the M symmetry direction of the square Brillouin zone respectively. The small gray vectors represent the in-plane wavevector of the

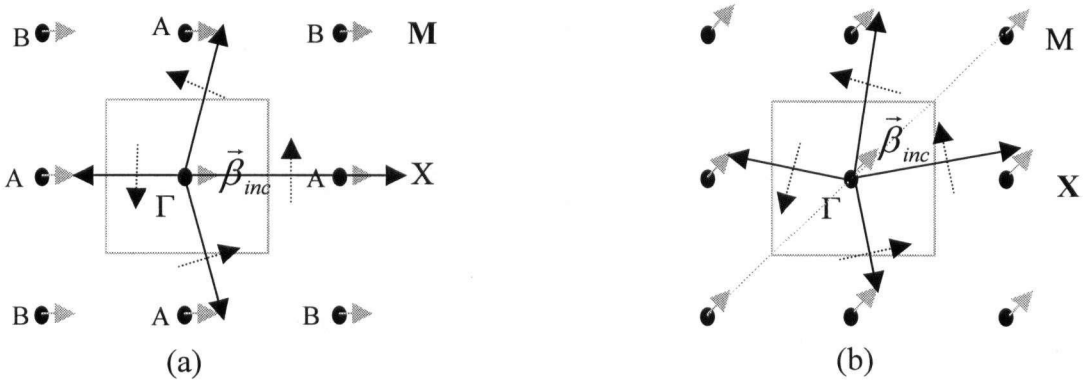

Figure 2.3: Momentum space diagram for a square lattice. The gray square represents the first Brillouin zone of the square lattice. Figures (a) and (b) represent cases where the incident radiation is along the X symmetry direction and the M symmetry direction of the square reciprocal lattice respectively. The dots represent the Fourier components of the dielectric scattering potential. The small gray vectors represent the in-plane wavevector of the incident radiation. The large vectors represent the in-plane wave vectors of the field components that result from the scattering potential adding momentum to the incident field. The polarization of each field component is represented by small dashed vectors. In (a) the 1st order Fourier components are labeled by A, and the 2nd order by B. The component at the center of the Brillouin zone is the 0th order or radiative component [1,3].

incident radiation. The large vectors represent the in-plane momenta of the scattered wave components that result from the scattering potential adding in-plane components to the incident field's momentum. The polarization of each field component is represented by small dashed vectors for the case of the s-polarized (TE-like) scattered field components. There are a duplicate set of p-polarized (TM-like) scattered field components (not shown). In Fig. 2.3 (a) the 1st order Fourier components are labeled by A, and the 2nd order are labeled by B. The component at the center of the Brillouin zone is the 0th order or radiative component that couples to radiation fields.

The zone-folded dispersion for a weak 2D texture with square symmetry was well described in [3,1]. Generally, for a given incident wavevector $\vec{\beta}_{inc}$, the Fourier components of

the square lattice texture scatter the incident field into a discrete set of scattered states with in plane wave vectors $\vec{\beta}_{inc} + \vec{G}_m$, where $\vec{G}_m = i\beta_g \hat{x} + j\beta_g \hat{y}$. When the incident frequency corresponds to one of the slab modes at these in-plane wave vectors, $\omega(\left|\vec{\beta}_{inc} + \vec{G}_m\right|)$, the amplitude of the corresponding fields will be resonantly enhanced. This resonant field affects the specular reflectivity over a range of frequencies in the vicinity of this phase-matched condition. The dispersion is a function of β_{inc} , which is schematically illustrated for the lowest order resonant slab modes in Figure 2.4. The mode at $\omega(\left|\beta_{inc}\hat{x} + \beta_g \hat{x}\right|)$ increases monotonically

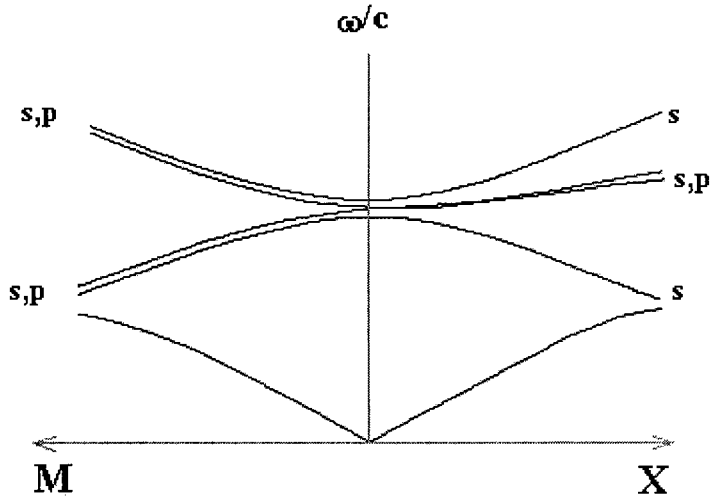

Figure 2.4: Schematic dispersion diagram for a 2D square lattice texture in a thin slab waveguide. The s and p are the polarizations labels of the photonic modes.

in energy as $\vec{\beta}_{inc}$ increases along the X direction. This mode corresponds to the highest upward dispersing band in Figure 2.4. The mode excited at $\omega(\left|\beta_{inc}\hat{x} - \beta_g \hat{x}\right|)$ decreases monotonically in energy as $\vec{\beta}_{inc}$ increases in the X direction, which corresponds to exciting the lowest, downward

dispersing band in Figure 2.4. The modes at $\omega(|\beta_{inc}\hat{x} \pm \beta_g \hat{y}|)$ disperse upward in energy as $\vec{\beta}_{inc}$ increases in the X direction, but at a moderate rate compared to the other two modes.

The polarization labels on the bands shown in Figure 2.4 can be understood using the following symmetry argument. The polarization (s, p or elliptical) density of the radiation of the 0^{th} order component that determines the coupling to the radiative fields is given by (2.1) [1]

$$\vec{P}(\vec{\beta}_{inc}) = \sum_{m=1...N} \chi(\vec{G}_m)\vec{E}(\vec{\beta}_{inc} - \vec{G}_m) \qquad (2.1)$$

(here N=4 when only considering the first order Fourier components of the scattering potential). Under resonant excitation conditions, one or two Fourier components of the field corresponding to the resonantly excited TE slab modes will dominate the scattered field everywhere except at $\vec{\beta}_{inc} = 0$. The upward dispersing mode in Figure 2.4 becomes dominated by a single Fourier component as it moves away from the zone centre, the component in the $\hat{x}$ direction. This corresponds to a TE slab mode at $(\beta_{inc} + \beta_g)\hat{x}$, which is polarized in the $\hat{y}$ direction. From Equation 2.1 above, the polarization density at $\vec{\beta}_{inc}$ is polarized in the $\hat{y}$ direction, thus generating an s-polarized radiation field in the upper half space. The downward dispersing mode in Figure 2.4, becomes dominated by a single Fourier component, the component in the $-\hat{x}$ direction. This corresponds to a TE slab mode at $(\beta_{inc} - \beta_g)\hat{x}$, which is also polarized in the $\hat{y}$ direction, so the polarization density at $\vec{\beta}_{inc}$ is polarized in the $\hat{y}$ direction. This again generates an s-polarized radiation field in the upper half space. For the two moderately dispersing bands things are different and slightly complicated. From symmetry, the incident field must excite either symmetric or anti-symmetric combinations of these slab modes (degenerate in the absence of texture) at $\vec{\beta}_{inc} \pm \beta_g \hat{y}$. It is evident that the magnitude of the

wavevectors of each of these components become bigger slowly when $\vec{\beta}_{inc}$ increases in the X direction, so these modes experience relatively little dispersion. A symmetric superposition of these scattered slab modes will add as shown in Equation 2.1 to yield a polarization density at $\vec{\beta}_{inc}$ oriented along the $\hat{y}$ direction, corresponding to s-polarized radiation in the upper half space, while the anti-symmetric combination leads to a polarization density oriented parallel to $\vec{\beta}_{inc}$, which can only lead to p-polarized radiation in the upper half space. Similarly when $\vec{\beta}_{inc}$ is oriented along the M direction, it follows that there are 2 s- and 2 p-polarized modes, one each dispersing up and down. That is how the polarizations are labeled in Figure 2.4. More generally, if $\vec{\beta}_{inc}$ is away from these high symmetry lines in the Brillouin zone, the eigenmodes are no longer purely symmetric and anti-symmetric superpositions of the untextured modes. These modes are, in general, elliptically polarized, and cannot be labeled as pure s- or p-polarized.

For the second harmonic generation, in addition to enhancements of the magnitude, it is important to understand the polarization conversion rules [22]. These conversions are sensitive to the symmetries and relative orientations of the photonic and electronic lattices. In this thesis, the nonlinear waveguide used is the semiconductor material GaAs, and the photonic crystal has square symmetry. The GaAs crystal is of cubic symmetry, and a member of the $\bar{4}3m$ point group. For some specific relative orientations, no s or p polarizations can be excited in the second harmonic [22]. But for arbitrary orientations of the two lattices, either s or p-polarized incident radiation will in general produce an elliptically polarized second harmonic field.

2.3 Theory Behind the Linear and Non-linear Reflectivity Models

2.3.1 Linear Model

Previous work in our lab has developed a Green's function based solution to Maxwell Equations. The solutions yields a linear model [1,2] for efficiently determining the specular reflectivity spectrum of two dimensionally textured slab waveguides. The results of this computer code have been validated by verifying model predictions with several experimental results [3]. The code can model the reflectivity spectrum of structures, like that in Figure 2.5, that contain any number of layers, including semi-infinite upper and lower layers. It can handle any angle of incidence for plane waves (incident angle θ and azimuthal angle φ) on the surface of the waveguide, for arbitrary

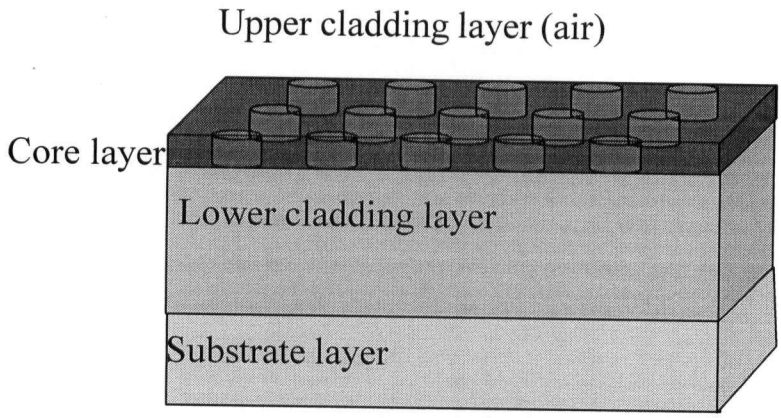

Figure 2.5: Schematic diagram of a planar waveguide textured with a 2D square grating.

polarizations. An outline of the formalism used in this linear model is provided below, in order to familiarize the reader with concepts central to understanding the nonlinear results presented below.

When a plane wave is incident on the surface of a textured planar waveguide with a well-defined in-plane wavevector, $\vec{\beta}$, the incident field in the upper half space can be represented as [1,2]

$$\vec{E}_{inc}(\vec{\beta}, z) = \vec{E}_o e^{-i\omega_0 z} e^{i\vec{\beta}\cdot\vec{\rho}} \qquad (2.2)$$

where $\omega_0 = \sqrt{\tilde{\omega}^2 - \vec{\beta}^2}, \tilde{\omega} = \omega / c$, and $\vec{\rho} = x\hat{x} + y\hat{y}$. The incident plan wave is assumed to have unit amplitude, and it may have any transverse polarization. Because the grating has a well-defined 2D periodic texture represented by reciprocal lattice vectors, $\{\vec{G}_m\}$, the electric field in the grating can be expressed as [1,2]

$$\vec{E}(\vec{\rho}, z) = \sum_m \vec{E}(\vec{\beta} + \vec{G}_m; z) e^{i(\vec{\beta}+\vec{G}_m)\cdot\vec{\rho}} \qquad (2.3)$$

For an abitrary $\omega, \vec{\beta}$, the non-specular field $\{\vec{G} \neq 0\}$ components in Equation 2.3 will be small. But, when $\omega, \vec{\beta}$, coincide with one of the allowed leaky eigenstates of the 2D textured planar waveguide, one or more of the scattered field components in Equation 2.3 becomes large. Depending on the linewidth, or inverse lifetimes of these modes, the scattered field strength can become very large, much larger than the incident field amplitude. In this thesis the emphasis is on fairly low-energy bands that can be quite accurately described by retaining only a sub-set of the smallest Fourier components in Equation 2.3. The zeroth order component is the one responsible for coupling light into and out of the guided modes of the waveguide.

For a slab waveguide, we need to solve the inhomogeneous Maxwell equations (2.4) [1]

$$\nabla \cdot \vec{D}(\vec{r}) = 0$$

$$\nabla \times \vec{B}(\vec{r}) + \frac{i\omega}{c}\vec{D}(\vec{r}) = 0$$

$$\nabla \cdot \vec{B}(\vec{r}) = 0$$

$$\nabla \times \vec{E}(\vec{r}) - \frac{i\omega}{c}\vec{B}(\vec{r}) = 0 \qquad (2.4)$$

Here we are only concerned with the linear response of nonmagnetic materials, so μ=1 and $\vec{H}(\vec{r}) = \vec{B}(\vec{r})$. The displacement field is given by (2.5) and the total linear polarization is given by (2.6)

$$\vec{D}(\vec{r}) = \vec{E}(\vec{r}) + 4\pi\vec{P}^{tot}(\vec{r}) \qquad (2.5)$$

$$\vec{P}^{tot}(\vec{r}) = \chi(\vec{r})\vec{E}(\vec{r}) \qquad (2.6)$$

The total linear susceptibility, $\chi(\vec{r})$, is divided into two components ,

$$\chi(\vec{r}) = \chi_s(z) + \Delta\chi_g(\vec{\rho}, z) \qquad (2.7)$$

where $\chi_s(z)$ represents the linear response of the untextured slab waveguide, and $\Delta\chi_g(\vec{\rho}, z)$ describes the deviation from $\chi_s(z)$ in the textured region. Now the inhomogeneous Maxwell equation can be written in the form (2.8)

$$\nabla \cdot (\varepsilon_s(z)\vec{E}(\vec{r})) = -4\pi\nabla \cdot \Delta\vec{P}_g(\vec{r})$$

$$\nabla \times \vec{B}(\vec{r}) + i\tilde{\omega}\varepsilon_s(z)\vec{E}(\vec{r}) = -4\pi i\tilde{\omega}\Delta\vec{P}_g(\vec{r})$$

$$\nabla \cdot \vec{B}(\vec{r}) = 0$$

$$\nabla \times \vec{E}(\vec{r}) - i\omega\vec{B}(\vec{r}) = 0 \qquad (2.8)$$

where $\varepsilon_s(z) = 1 + 4\pi\chi_s(z)$, and $\Delta\vec{P}_g(\vec{r}) = \Delta\chi_g(\vec{r})\vec{E}(\vec{r})$ [1]. A crucial aspect of this model is that the textured layers are always assumed to be much thinner than the wavelength of light, hence the z variation of the field components over the grating can be neglected. This means that when a plane wave with frequency $\tilde{\omega} = \omega / c$ and in-plane wave vector $\vec{\beta}_{inc}$ is incident from the upper half-space, the self-consistent solution for a single Fourier component of the field in the grating is given by (2.9)

$$\vec{E}(\tilde{\omega}, \vec{\beta}_i) = \vec{E}^{\text{hom}}(\tilde{\omega}, \vec{\beta}_i) + \vec{g}(\tilde{\omega}, \vec{\beta}_i) \times \sum_j \vec{\chi}_{ij}^{(1)}(-\tilde{\omega}, \tilde{\omega})\vec{E}(\tilde{\omega}, \vec{\beta}_j) \quad (2.9)$$

where $\vec{g}(\tilde{\omega}, \vec{\beta}_i)$ is the Green's function solution of equation (2.8) and $\vec{E}^{\text{hom}}(\tilde{\omega}, \vec{\beta}_i)$ is the corresponding homogeneous solution. There is no z-dependence left in Eqn. 2.9, $\vec{\beta}_i = \vec{\beta}_{inc} - \vec{G}_i$ is the in-plane wave vector of the Fourier component being solved for, and the $\vec{\chi}_{ij}$ are the coefficients of the Fourier expansion of the periodic susceptibility ($\vec{\chi}_{ij} = \int d\vec{\rho}\Delta\vec{\chi}(\vec{\rho})e^{[-i(\vec{G}_i - \vec{G}_j)\cdot\vec{\rho}]}$). Eqn. 2.9 is a self-consistent equation for the Fourier components of the field in the gratings. It can be solved by matrix inversion. Once the exact field in the grating is determined from Eqn. 2.9, the field elsewhere can be easily obtained using another Green's function that independently propagates each Fourier component of the grating polarization into the surrounding (untextured) medium. This, in particular, is how the reflected field amplitude is obtained from the zeroth order component of the solution obtained from Eqn. 2.9. The number of Fourier components used in the simulations play an important role in determining the accuracy of the simulations, especially the higher energy bands. Generally, 4 nearest-neighbor rings (81 components) are sufficient to accurately converge for the lowest 8 bands. In order to obtain more accurate

simulation results for the high-lying bands relevant to the second harmonic out-coupling, 6 rings (169 Fourier components) were used in this work.

2.3.2 Non-linear Model

The linear model described above has subsequently been generalized by others in the group to treat a number of nonlinear optical processes involving textured, planar waveguides. [22,30]. In this section the model that treats second harmonic generation is briefly described.

Using the Fourier field components of the field in the grating layer obtained from the linear model, the Fourier components of the second-order polarization in the same textured region are calculated as [22].

$$\vec{P}^{(nl)}(2\tilde{\omega},\vec{\beta}_n) = \sum_{m,l} \vec{\chi}_{nm}^{(2)}(-2\tilde{\omega},\tilde{\omega},\tilde{\omega}) : \vec{E}(\tilde{\omega},\vec{\beta}_{inc}-(\vec{G}_m-\vec{G}_l))\vec{E}(\tilde{\omega},\vec{\beta}_{inc}-\vec{G}_l) \quad (2.10)$$

$$\vec{E}(2\tilde{\omega},\vec{\beta}_n) = \vec{g}(\vec{\beta}_n,2\tilde{\omega}) \times [\sum_m \vec{\chi}_{nm}^{(1)}(2\tilde{\omega},2\tilde{\omega})\vec{E}(2\tilde{\omega},\vec{\beta}_m) + \vec{P}^{(nl)}(2\tilde{\omega},\vec{\beta}_n)] \quad (2.11)$$

Where the in-plane wave vectors of the 2nd order field components are $\vec{\beta}_n = 2\vec{\beta}_{inc} - \vec{G}_n$. Then both this nonlinear polarization and the linear polarization at $[(2\tilde{\omega},\vec{\beta}_n)]$ are used as driving terms to self-consistently calculate the Fourier components of the second-harmonic field in the grating using a similar Green's-function approach. The zeroth order component of the field at $2\tilde{\omega}$ is the one that generates the second harmonic field in the specular direction that is measured in the experiment (for the details, refer to [22]). The number of Fourier components of the second-harmonic used in the non-linear simulations is also very important in determining the accuracy of the second harmonic simulations. Since 6 rings (169 Fourier components of the fundamental) are used in the linear calculation, 3 rings (49 Fourier components of the second

harmonic) were used in the non-linear simulation for this work. A higher number of rings (7 rings, and 8 rings for the linear solution, and 4 rings for the non-linear fields) were also tried in the simulations, but no significant change of the band energies was observed.

2.4 Sample Design Procedure

If the square lattice textured waveguide is irradiated from above with light at a certain frequency ω and some arbitrary in-plane momentum $\vec{\beta}_{inc}$, the light will generally be transmitted without generating any enhancement of the fields in the textured core region of the guide (that is, the field strength in the core will be of the same order as the incident field). The second order polarization it excites in the waveguide, through a non-zero $\chi^{(2)}(-2\omega,\omega,\omega)$, would then be comparable to the second order field excited in the same but untextured waveguide. If the frequency 2ω and in-plane wave vector $2\vec{\beta}_{inc}$ of this nonlinear polarization do not coincide with one of resonant modes, then the polarization will also couple out of the guide in much the same way it would in the absence of texture. The overall second harmonic generation (SHG) conversion efficiency for this process in GaAs is small. If either or both of the fields at $(\omega,\vec{\beta}_{inc})$ and $(2\omega,2\vec{\beta}_{inc})$ coincide with the localized mode dispersion, the conversion efficiency can be significantly enhanced due to the excitation of strong local fields associated with excitation of resonant photonic modes of the textured waveguide at the fundamental frequency. The textured membrane can be thought of as a 1D micro-cavity, with additional modification of the photonic density of states provided by the strong 2D texture. Cavity modes that lie within the vacuum light cone couple to plane waves that radiate in the surrounding half-spaces. This radiative coupling determines the lifetimes, or the Q's of these cavity modes. Weakly coupled

modes with high Q's will accumulate significant local field intensities when excited from the vacuum. The advantage of this grating coupling geometry is that the total internal reflection that confines the dominant (evanescent) field components of the resonant eigenstates does not require the fabrication of multi-layer Bragg reflectors above and below the cavity layer. This confining mechanism, characteristic of these waveguide-based photonic crystals, is responsible for extremely large enhancements in the conversion efficiency [22].

The main purpose of this thesis is to design a two dimensional (2D) periodic texture on a thin GaAs semiconductor waveguide, on which we can get second harmonic enhacement while the energy of the second harmonic is less than the band gap energy of the GaAs. That ensures a truly virtual two photon process, uncomplicated by photo-electron processes. The band gap of GaAs is around 1.42 ev, or 11500 cm^{-1}. We therefore designed the sample so that 2ω should be near 10000 cm^{-1} (wavelength is around 1 μm). That means the light source at ω must be near 5000 cm^{-1} (wavelength of $\sim$ 2 μm). It also means that the PC should have a band of leaky photonic eigenstates at around 5000 cm^{-1}, and a corresponding band or bands at twice the in-plane momentum, with an energy of $\sim$10000 cm^{-1}. The second harmonic generation efficiency can be influenced either through the incoming resonance and/or the outgoing resonance. By properly designing the sample, the second harmonic conversion can be studied in a region where both the incoming and the outgoing resonance conditions occur together. The bands become densely spaced and complicated at higher energies. This can complicate the interpretation of the results, so we purposely chose the lowest s-polarized, downward dispersing leaky mode band in the sample as the in-coming resonance. This minimized the order of the higher energy bands that resonated with the second harmonic polarization.

The untextured planar GaAs waveguide consists nominally of a 140 nm thick core layer of GaAs supported on an ~1 μm thick cladding layer of $Al_{0.98}Ga_{0.02}As$ (A506). Based on the considarations stated above, and after running many linear dispersion simulations, a pitch of ~760 nm - 800 nm, and a hole diameter of ~300 nm - 360 nm, were chosen as the target parameters so that fundamental light at a wavelength of ~2 μm could resonantly excite the lowest order band of leaky photonic eigenstates characteristic of the strongly textured membrane. The linear simulations (see below) show that these parameters offer higher-energy bands that the 2nd order polarization might also resonantly drive, all at energies less than the band gap of GaAs of 11500 cm^{-1}. Figure 2.6 and Figure 2.7 show the linear simulation results (at 10°, 15°, 20°, 25°, 30°, 35°) for s and p polarizations for our experimental sample design. Shaded areas are the ranges of fundamental and second harmonic frequencies of interest. The incident light is chosen along the Γ-X direction of the photonic crystal. The parameters used in the simulation are listed in Table 2.1.

Table 2.1: Simulation parameters for the square lattice textured planar waveguide used in the second harmonic experiments

Parameter	Value
Pitch	770 nm
Hole Radius	160 nm
Core Thickness	140 nm
Oxide Thickness	950 nm
Hole Depth	140 nm

Figure 2.6 shows the calculated reflectivity spectrum of the designed sample along the Γ-X direction of the Brillouin zone for different incident angles. From this, and with reference to the schematic bandstructure in Fig. 2.4, the lowest s-polarized, downward dispersing band can be seen from 5500 cm^{-1} to 5200 cm^{-1} in the range 25° to 35°. At double the frequency, from roughly

10,200 cm^{-1} to 10,800 cm^{-1}, and at the same incident angles, there are relatively flat s- and p-polarized bands evident. This double frequency region is also less than the band gap of GaAs. These simulations suggest that the second harmonic generated by an s-polarized fundamental should exhibit an in-coming enhancement while the corresponding s- and p-polarized fields at the second harmonic have the opportunity to interact with relatively flat bands for incident angles between 25° to 35°. From Figure 2.7, the lowest p polarized band is higher than 6000 cm^{-1}. The second harmonic generated by exciting this band with the fundamental field would be higher than 12000 cm^{-1}, which is larger than the band gap of GaAs, so this sample is not compatible with trying to cleanly observe second harmonic enhancement when exciting with p-polarized fundamental fields.

In summary, based on the simulations results presented here, we attempted to fabricate a sample with a pattern having the parameters listed in table 2.1. This sample was expected to enhance the second harmonic generated when excited by s-polarization and detected either in s- or p-polarizations. Additional influences on the conversion due to out-going resonant excitation of the higher lying s- and p-polarized bands were expected for incident angles between 25° to 35°.

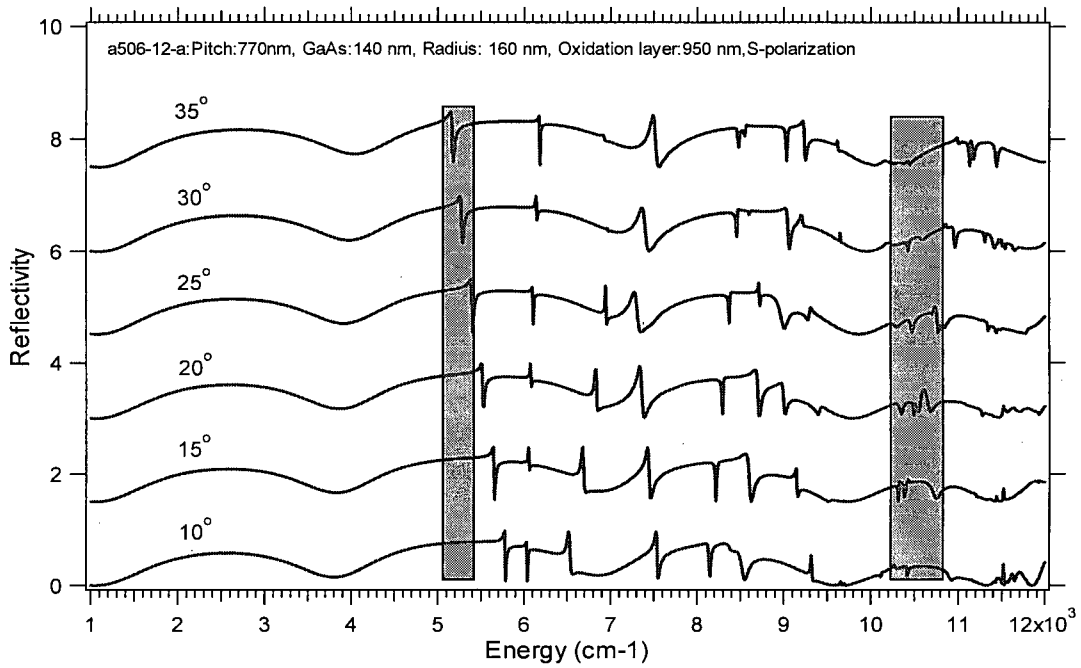

Figure 2.6. Simulated reflectivity results for s polarized light incident along the Γ-X direction of the photonic crystal described in Table 2.1. Shaded areas are the ranges of fundamental and second harmonic frequencies of interest.

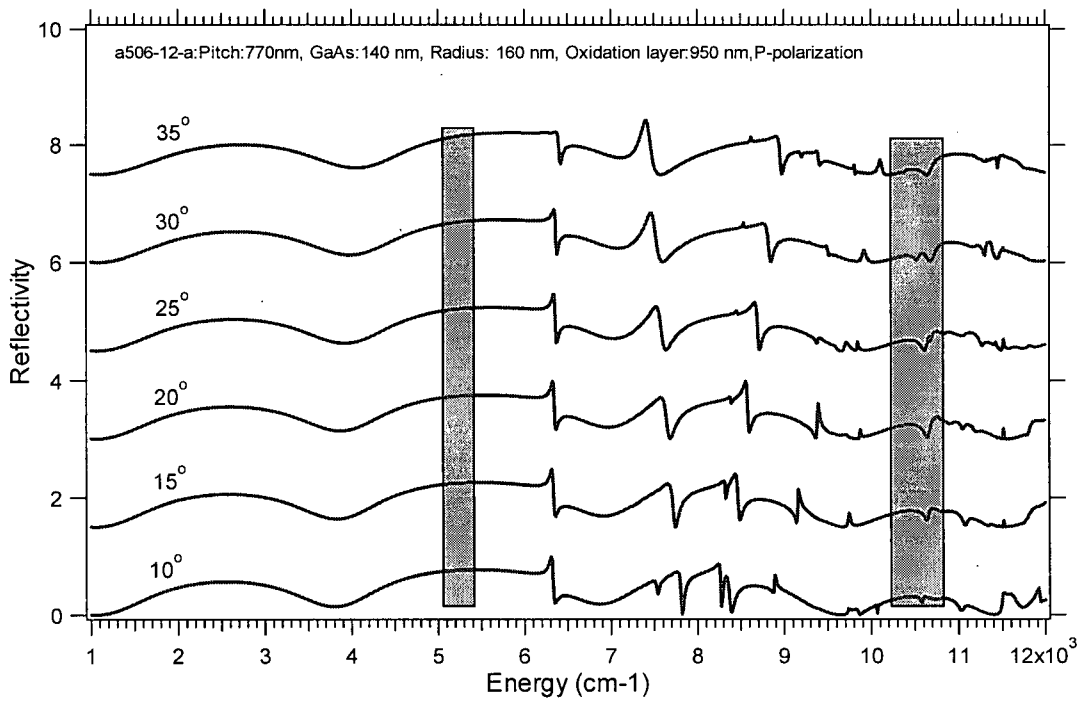

Figure 2.7. Simulated reflectivity results for p polarized light incident along the Γ-X direction of the photonic crystal described in Table 2.1. Shaded areas are the ranges of fundamental and second harmonic frequencies of interest.

The preceding discussion concerning the polarization of the in-coming and out-going fields only implies that the photonic eigenmode enhancements *might* be observed if the fundamental can generate both s- and p-polarized polarization fields in the GaAs at the second harmonic. This is by no means guaranteed if the photonic crystal axes are aligned with the principal axes of the underlying GaAs crystal. In equation (2.10), the nonlinear susceptibility, $\tilde{\chi}^{(2)}(-2\omega,\omega,\omega)$, is a second order tensor. The GaAs has cubic symmetric and is characterized by the $\bar{4}3m$ point group. When the [001] axis of the GaAs crystal is aligned with the X axis of the square symmetric photonic lattice, it is not possible to excite p-polarized second-harmonic modes along the Γ-X direction of the square Brillouin zone. Likewise, for the same orientation of the two lattices, no s-polarized second harmonics are generated along the Γ-M direction. The sample was therefore fabricated so that the Γ-X direction of the photonic crystal is rotated by 20° with respect to [011] direction of the GaAs electronic crystal. By reducing the symmetry of the combined electronic-photonic system in this way, both s- and p- polarized second harmonic polarizations are allowed.[22]. A schematic diagram of the relative crystal orientations is shown in Figure 2.6.

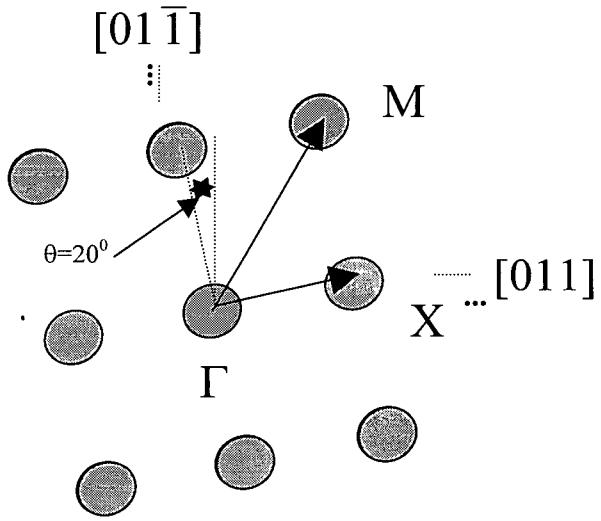

Figure 2.6: A schematic diagram of the photonic crystal with a square lattice (filled dots) rotated by 20° with respect to the [011] direction of the GaAs electronic crystal.

Chapter 3

Sample Fabrication

This chapter describes how the samples were fabricated by the author. The procedure consists of the following processing steps: cleavage, pre-cleaning and drying, spin coating the resist layer, e-beam lithography, developing, etching, and oxidation. The apparatus and nominal process parameters used to fabricate the samples were previously developed by others in the lab, with the exception of the electron beam lithography system. The author was responsible for transferring the electron beam lithography equipment from an Hitachi scanning electron microscope (SEM) with a field emission source, to a JEOL 840A system with a thermal emitter, and calibrating all of the settings on the new machine.

Table 3.1 summarizes the physical parameters of the epitaxial wafer used to fabricate the photonic crystal samples schematically represented in Figure 2.3. It was grown using molecular beam epitaxy (MBE) by Dr. Shane R. Johnson from Arizona State University. The 1.0 μm thick $Al_{0.98}Ga_{0.02}As$ layer was grown on a 100 μm thick GaAs (100) substrate; then the single core layer of GaAs ~140 nm thick was grown on the $Al_{0.98}Ga_{0.02}As$ layer.

Table 3.1 The nominal physical parameters of the epitaxial wafer used to fabricate the photonic crystal samples

Crystal orientation	(100)
Core layer (GaAs)	155 nm
Lower cladding layer ($Al_{0.98}Ga_{0.02}As$)	1000 nm
Substrate layer (GaAs)	100 μm

In order to fully utilize the planar waveguide wafer, it is cleaved into smaller samples, ~ 5 mm x 5 mm, before processing. The direction of cleavage surface is [011]. Before the samples are coated with resist, the surface of these slab waveguides must be carefully cleaned with acetone and methanol and totally dried by piping dry nitrogen on it.

3.1 Spin coating

PMMA, Poly(methyl-methacrylate), with a molecular weight of 950K was used for fine lithography because of its high resolution[4]. The 4% (by volume) PMMA is obtained by dissolving PMMA in a chlorobenzene solution. About 3 or 4 drops of 4% PMMA is applied to the sample. The samples were spun at 500 rpm for 10 seconds and then spun at 8,000 rpm for 40 seconds, yielding a thickness of approximately 200 nm. Finally the samples are baked on a hot plate at 175°C for at least 2 hours. This process bakes off the solvents in the PMMA. After baking, several marks were made on the each of the corners of the sample using a hard carbon pencil, and then dry nitrogen was applied to blow away the larger carbon particles on the surface. Some small carbon particles are left on the edges to help obtain a good focus under the SEM.

3.2 Electron Beam Lithography

A JEOL JSM-840A computer-controlled thermal-emission SEM was used to perform the lithography on the GaAs samples. The computer control system had to be transferred from an Hitachi 4100 field-emission SEM that was previously used for lithography. The advantage of the JEOL-based system is that it is a dedicated lithography tool with relatively stable emission current, compared to the Hitachi, which is a general purpose SEM with a noisy cold-cathode

emitter. Because the pattern size and uniformity are determined by the exposed current dose, the stable emission current is very important, especially when a long time is needed for making a specific pattern. The author was responsible for transferring the electron beam lithography equipment from a Hitachi SEM to a JEOL 840A SEM. Calibrations of both the magnification and the aspect ratio were performed several times using a commercial Cu mesh to ensure the best precision [5]. This step was very important for implementing the exact design of our sample.

The first step in the lithography process is the creation of a data file containing the exposure coordinates for the designed photonic crystal lattice. This Fortran-generated sq800.dat file (the file contains an array of x, y coordinates where the beam is to be directed) is then converted, using DCFILES.EXE, to a sq800.dc2 file (ASCII file) that can be recognized by the Lithography software (NPGS). This NPGS software controls the SEM beam to make a pattern in the PMMA by exposing it at pre-determined coordinates with a specified dose. Because PMMA is a positive resist, the electron beam breaks many of the bonds of the large PMMA molecular chains, so that they are more soluble in the developer than the unbroken (unexposed) chains. The longer the electron beam exposes a particular location during lithography, the more chains in a larger area will be broken, and this results in a larger hole once developed. Generally the desired pattern is written several times on different areas of the resist using a range of current doses in order to obtain at least one with the desired features for the experiment. The typical exposed area is a 90 μm x 90 μm square at the highest magnification used for lithography (1,000 times). In order to get the best results, it is necessary to do the initial focus adjustments of the SEM at very high magnification of 50,000 times, using the small carbon particles left by pencil marks on the very edges of the samples. In this process, the sample holder stage controls are adjusted to ensure that the sample piece is as level as possible, so many patterns can be made without re-focusing.

Then the magnification is set to 1000 times and the electron beam is moved to the sample to begin the writing processing. The final consideration is where to place the "beam dumps", where the beam is directed when not sequencing through the specified array of exposure points. If the beam dump is on the just-written pattern, it will overexpose and damage it. In order to solve this problem, the sq800.dc2 can be opened, viewed, and modified by DC.EXE. In this software, we can set the beam dump to be outside of the pattern, in order to not damage the written pattern [32]. The beam dump was usually set 5 μm away from the edge of the patterned region of the sample.

Table 3.2 lists the typical parameters of the SEM used in e-beam lithography to fabricate the samples used in this thesis. After 20 minutes of stabilization, the e-beam current directed on the pattern, which is monitored by an external electrometer, is set at 15 pA, or even lower. Although it requires a longer time to write a pattern at such a small current, the resolution is much better than that obtainable using larger e-beam currents. Higher e-beam current can be chosen to decrease the e-beam time, but at the expense of losing resolution. After each pattern is written, the x and y direction knobs, which control the movement of the translation stage of the SEM, are adjusted to move the sample to the next position to write a new pattern. After the sample is moved to a new selected position, the e-beam lithography is started immediately by pressing the "Enter" key. The time to write a typical pattern is ~20 minutes.

The exposed PMMA can be removed using the developing recipe shown in Table 3.3. The MIBK in the table is Methyl Isobutyl Ketone diluted in Isopropyl Alchohol (IPA). The volume Ratio of MIBK:IPA is 1:3. At this stage the PMMA resist has been transformed into an etching mask. The developed sample is checked under an optical microscope to make sure it is

properly and evenly exposed. At this point of the processing the exposed squares should look uniformly brighter than the unexposed regions of the surrounding resist.

Table 3.2: Typical SEM parameters used in e-beam lithography

Aperture	3
Probe Current	$6x10^{-11}A$
Working Distance	39 mm
Accelerating Voltage	20.0 KV
Electrometer current	$1.5x10^{-11}A$
Emission Current	50 μA
Filament Current	225 μA

Table 3.3: Developing recipe for PMMA.

Chemical	Time
MIBK	90 sec
Propanol	30 sec
DI Water	30 sec
Oxyethylmethenol	15 sec
Methanol	30 sec

3.3 Plasma Etching

A Plasma Quest electron-cyclotron resonance (ECR) plasma etcher is used to transfer the pattern in the PMMA into the underlying GaAs layer. By delivering microwave radiation resonant with the cyclotron frequency of electrons, the ECR creates a plasma in a low pressure gas (10^{-2} Torr). During etching, the sample sits on a liquid cooled chuck. The temperature of the chuck is kept at 5 ° C by cycling cooled liquid to prevent the sample from overheating when exposed to the plasma process. Under the presence of a strong, static magnetic field, the ions

from the plasma cloud, which are driven by a radio frequency (RF) bias on the sample chuck, are accelerated along the magnetic field to strike the sample normal to the surface, where they etch the exposed GaAs and PMMA kinematically and chemically. The specific etch recipe used is shown in Table 3.3 [6,3]. The etch rate in the GaAs is approximately 100 nm per minute. It is essential to etch all the way through the GaAs layer in order to oxidize the underlying AlGaAs layer, so the etch is made longer than nominally required to get just through the GaAs. The PMMA is also etched, but the etching time is so short that the PMMA can not be fully etched away. After the etching, the sample has some PMMA left on the top of the GaAs. The remaining PMMA can be washed away by stirring the sample first in acetone and then in methanol. If there is still PMMA left, the latter process is repeated. Finally, the cleaned sample is blown dry by directing a flow of dry Nitrogen on the surface.

Table 3.4: ECR recipe for etching

Cl_2 flow	2.0 sccm
BCl_3 flow	2.0 sccm
Ar flow	20.0 sccm
Microwave power	100 Watts
RF Bias voltage	100 Volts
RF Power	25 Watts
Chuck Temp	5 ° C
Process Pressure	10 mTorr
BacksideHe pressure	5 Torr
Time	125 sec

The etched patterns are then imaged using the SEM. Figure 3.1 lists typical hole sizes corresponding to various e-beam doses. In Figure 3.1, the patterns are square lattices with pitchs of ~770 nm. The error bar for each measurement is ± 20 nm, which is the limit to which the diameters can be determined from the SEM images. The dotted line is a linear fit to the data. We

can see that basically the radius increases linearly with increased e-beam dose, but there is an offset. The fluctuation of the points is because of the drift of the e-beam current.

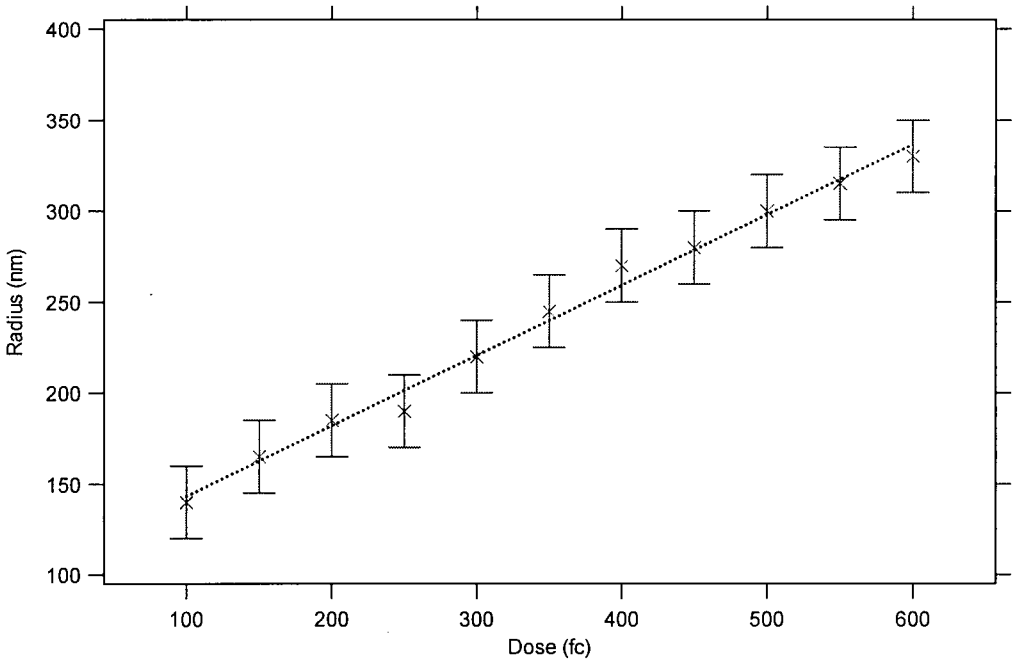

Figure 3.1 Hole radius corresponding to different e-beam doses. The ordinate is the hole size of the sample. The abscissa is the e-beam dose used to make such a hole size.

3.4 Oxidation

The final step of the sample fabrication is oxidation. This step converts the bottom cladding layer of $Al_{0.98}Ga_{0.02}As$ to alumina, so its refractive index can be reduced from ~3.6 to around 1.6. The oxidation set up was designed and assembled by Vighen Pacradouni, a former Ph.D. student, and Francois Sfigakis, a former Masters student. [7]. The sample is sealed in a quartz tube situated in a furnace, then the quartz tube is purged with dry nitrogen for ~ 1 hour. Subsequently the temperature is increased from room temperature to 425 °C in a period of 30 minutes, as controlled by a digital programmer on the furnace. The temperature is then held at 425 °C for 5 minutes, during which time 100 sccm of nitrogen is bubbled through 95 °C water

and directed through the furnace tube. This water steam-oxidizes the aluminum-containing alloy layer through the etched holes. Several test samples were lithographed, etched and oxidized before determining that after the 5 minutes oxidation period, a large flow of dry nitrogen from the bypass must replace the moist flow to purge the moisture out of the furnace. If this procedure is not followed, the sample "overoxidizes", with the alumina layer delaminating from the GaAs substrate. After the flows are exchanged, the temperature is reduced at a rate of 30 °C per hour until reaching room temperature.

3.5 Processing Summary

Experience has shown that there are many subtle details of the fabrication process that must be appreciated in order to routinely obtain good samples. First, much care has to be taken ensuring that the sample is as level as possible on the sample stage. Typically one writes several identical patterns using a bracketed set of doses (nominal dose plus and minus ~ 10%), to optimize the chances of obtaining one with the desired properties. If the sample is not flat, different patterns will come in and out of focus as the translation stage is moved. Second, the astigmatism and focus adjustments must be close to perfect. If the astigmatism is not removed, the holes will not be circular. When the focus is not good, the hole size will also be irregular. If these issues are patiently addressed, then the holes are round and their size scales in proportional to the dose applied.

Another key issue that should be noticed is the oxidation time. The best condition is to make the oxidized area slightly larger, ~ 2 μm, than the patterned square . If properly oxidized, the whole oxidized pattern and the oxidized part of the surrounding area are very smooth and

even. Over-oxidization results in nonuniform strain relief between the GaAs and Al_3O_2 that causes the interface to deform. Figure 3.2 is an SEM picture of a "good-quality", completed sample. The hole size and depth are very even and close to circular. The pitch of this square lattice is ~800 nm, the diameter of the air holes is ~400 nm, and the depth of etched hole is ~150

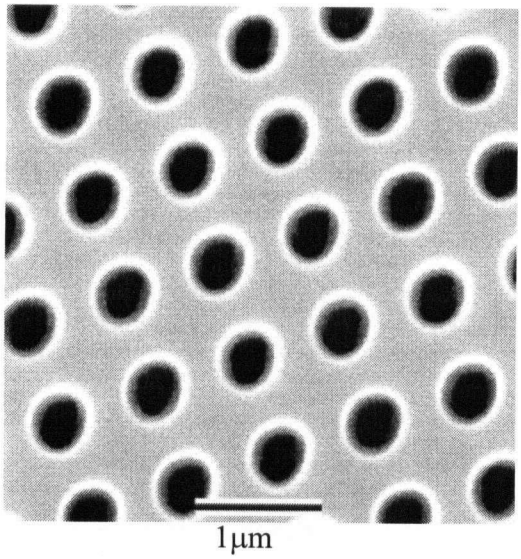

Figure 3.2 An SEM picture of a complete sample made under close-to-ideal conditions. The pitch of this square lattice is ~800 nm, the diameter of the air hole is ~400 nm, and the depth of etched hole is ~150 nm. The Γ-X direction of the pattern is rotated 20° relative to the cleavage face. A pattern like this was used for the optical experiments described in the next chapter.

nm. The Γ-X direction of the pattern is rotated 20° relative to the cleavage face. A pattern like this was used in the optical experiments described in the next chapter. Figure 3.3 is an SEM picture of the pattern with not very good focus, without astigmatism, good dose, without oxidation and imperfect leveling. The pitch of this square lattice is ~800 nm, the diameter of the air hole is ~300 nm, and the depth of etched hole is ~150 nm. The hole shapes are not particularly circular and the surface is quite rough.

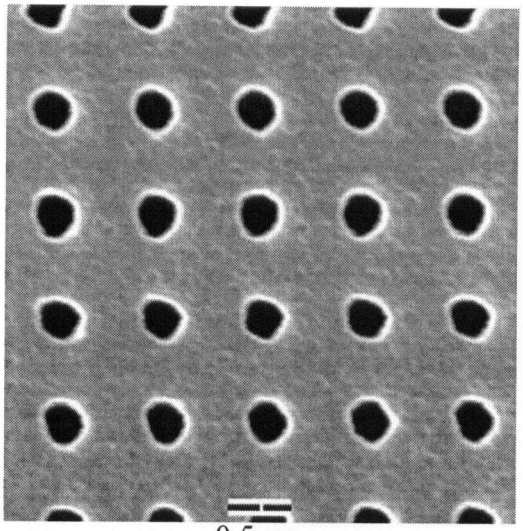

Figure 3.3 An SEM picture of a completed sample of less than ideal quality. The pitch of this square lattice is ~800 nm, the diameter of the air hole is ~300 nm, and the depth of etched hole is ~150 nm.

Figure 3.4 is an SEM picture of a sample that received too high a dose. The pitch of this square lattice is 800 nm, the diameter of the air hole is >800 nm, and the depth of etched hole is ~150 nm. Figure 3.5 is an SEM picture of an unoxidized sample showing the results of poor focus and astigmatism. The pitch of this square lattice is 800 nm, and the depth of etched hole is ~150 nm.

Figure 3.6 is an SEM picture of several patterns from a reasonably good-quality sample, after oxidation. Each bright square is 90 μm on a side, and the darkest regions are those where the underlying alloy is oxidized. There are several randomly located dark regions where the sample has oxidized through defects in the GaAs layer of the wafer. These defects are formed when growing GaAs wafer using MBE. This degree of oxidation is close to the limit: any further oxidation would lead to delamination and a rough surface.

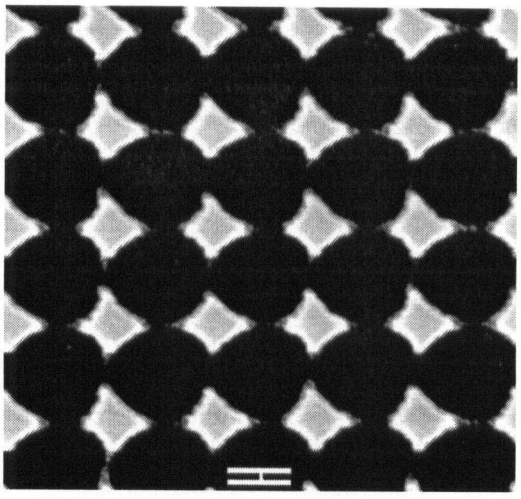

Figure 3.4 An SEM picture of an unoxidized pattern with good focus, without astigmatism, good leveling, but over dosed. The pitch of this square lattice is 800 nm, the diameter of the air hole is >800 nm, and the depth of etched hole is ~150 nm.

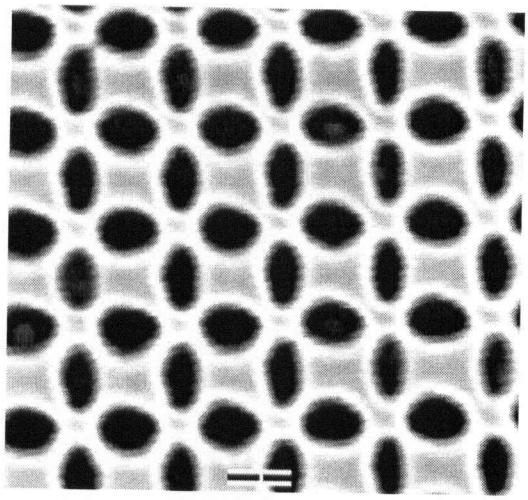

Figure 3.5 The SEM picture of the pattern with imperfect focus, with astigmatism, good dose, and without oxidation. The pitch of this square lattice is 800 nm, and the depth of etched hole is ~150 nm.

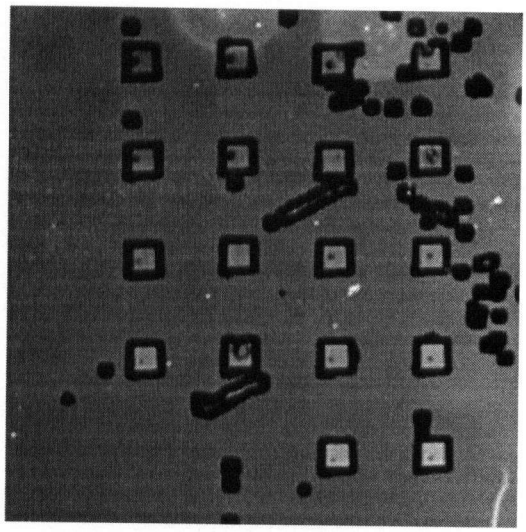

Figure 3.6 A low magnification SEM micrograph of a set of reasonably good-quality patterns after oxidation. The dark square around each pattern represents the oxidized part under each pattern. Other, randomly located dark shapes represent oxidized areas under defects in the GaAs wafer. Each bright square is 90 μm on a side.

Chapter 4

Results and Discussion

This chapter presents the results of linear and non-linear light spectroscopy experiments on a sample fabricated very close to the specifications defined in chapter 2. The experimental data are compared with linear and non-linear simulations based on the models described in Chapter 2. Section 4.1 presents results of the linear measurements and simulations. These focus on the dispersion and polarization properties of the lowest order leaky bands. Starting with the nominal parameters of the sample as determined by SEM images and provided by the wafer supplier, the optimized parameters of the photonic crystals were obtained by fitting the experiment results and the simulation results. From the linear dispersion curves for the lowest band (fundamental frequency, ~ 2 μm) and the higher order bands (second harmonic, ~1 μm) the most probable condition for getting resonant to resonant second harmonic enhancement was predicted. The sample was then sent to the University of Toronto, where Jessica Mondia of Professor Henry van Driel's group measured the angular dependence of the second harmonic reflected from it when irradiated by a fundamental in the frequency range of 1.5 μm to 2.0 μm.

Section 4.2 reports the results of this second harmonic experiment. Peak second harmonic enhancements of >1200 times were experimentally measured. The non-linear simulation results, obtained using sample parameters extracted from fitting the linear scattering spectra, are in remarkably good agreement with the experimental results, as discussed in Section 4.3. The s-polarized pump and p-polarized harmonic conversion results reveal the s-polarized incoming photonic mode dispersion and p-polarized outgoing photonic mode dispersion, with the greatest

enhancement in the second harmonic occurring where these two dispersion curves cross each other. Similar, but slightly more complicated effects are observed in the s-in, s-out polarization configuration.

4.1 Linear results

The linear reflectivity measurements were obtained using a Bomem DA8 Fourier Transform Interferometer (FTIR) in conjunction with a reflective-optic microscope in a θ–2θ set up designed and implemented by W. J. Mandeville, a former PhD student [3]. A schematic diagram of the optical layout is shown in Figure 4.1. There are three ellipsoidal mirrors (EM1, EM2, and EM3 with focuses of 10cm, 15 cm, and 150 cm, respectively) in the optics path to reflect, transmit, and focus the light into the Bomem. The output optical fiber has a diameter of 200 μm. A removable CCD camera is used to monitor and align the pattern at an intermediate image where a field stop is used to allow only the light reflected from the patterned part of the wafer to enter the spectrometer. A polarizer is positioned just in front of EM3 to control whether s or p polarized light is analyzed. The sample is fixed on the mount by vacuum grease and Teflon tape, and the rotation stages can be moved in concert to measure the specular reflection spectra for different normal (θ) and azimuthal (ϕ) angles. The Bomem FTIR spectrometer consists of a Michelson interferometer with a quartz beam splitter and an InGaAs detector, which can measure the spectrum from approximately 6,000 cm^{-1} to 13,000 cm^{-1}.

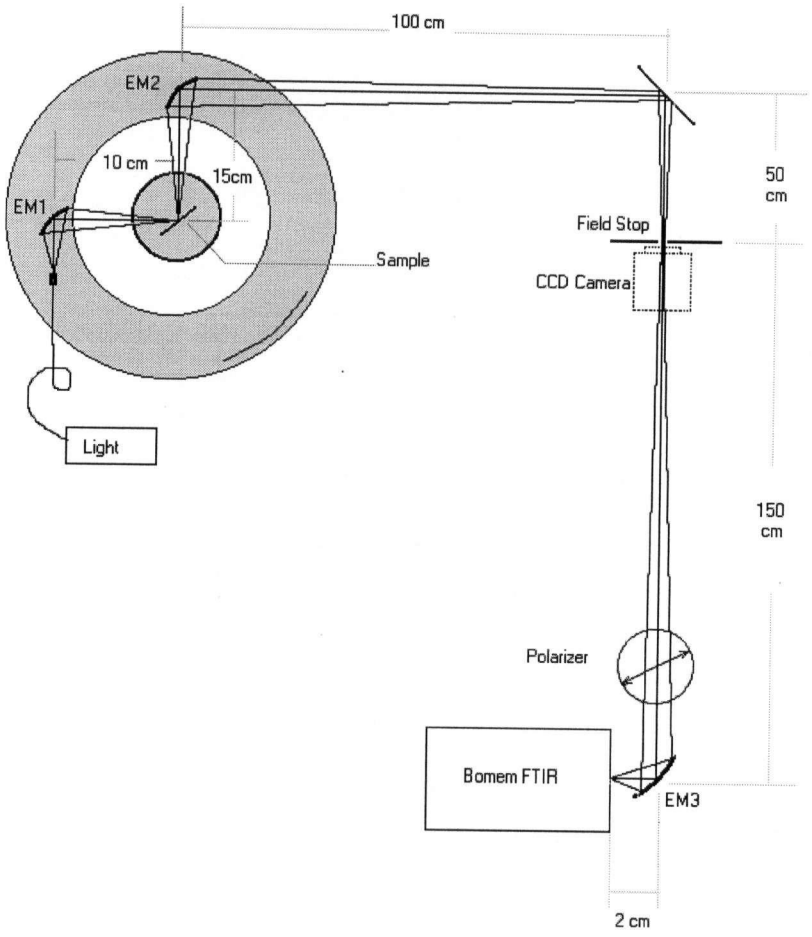

Figure 4.1: Schematic diagram of the optical layout used for linear reflectivity measurements.

Both s and p polarized specular spectra obtained with the incident beam along the Γ-X direction of the photonic crystal were measured at incident angles of 10^0, 15^0, 20^0, 25^0, 30^0, and 35^0. The measured and simulated spectra are shown in Figure 4.2.and Figure 4.3. The broad undulating features in all spectra are Fabry-Perot fringes, which are due to the interference of light reflecting on the top and bottom surfaces of the 950 nm oxide layer; they would be present in the absence of the 2D grating. The sharp Fano-like features indicate resonant coupling to a leaky slab mode attached to the textured waveguide. These resonances are narrower for modes

with long lifetimes and wider for modes with short lifetimes. The simulation parameters that provided the best fit for this square lattice textured planar waveguide sample are listed in Table 4.1. Figure 4.2 and Figure 4.3 compare the experimental and simulation results using the parameters listed in Table 4.1 for s and p polarizations respectively. Virtually all of the Fano features with predicted widths greater than ~ 50 cm^{-1} are in reasonably good agreement for the p-polarized data. Narrower features are never revealed in experiments on 90 μm x 90 μm patterns due to the fact that the simulations are for strict plane wave excitation, while specification of the in-plane momentum in the experiments is limited by the finite extent of the samples (and by the fact that the incident beam is not perfectly collimated). The agreement for the lowest lying s-polarized bands is also quite good, with the quality of the fits falling off at higher energies. It is important to note that the lowest order, downward dispersing leaky band near 6000 cm^{-1} is not evident in any of these spectra, which are limited in range due to the InGaAs detector.

Table 4.1: Simulation parameters for the linear code

Parameter	Value
Pitch	770 nm
Hole Radius	160 nm
Core Thickness	140 nm
Oxide Thickness	950 nm
Hole Depth	140 nm
Resolution	11 cm^{-1}

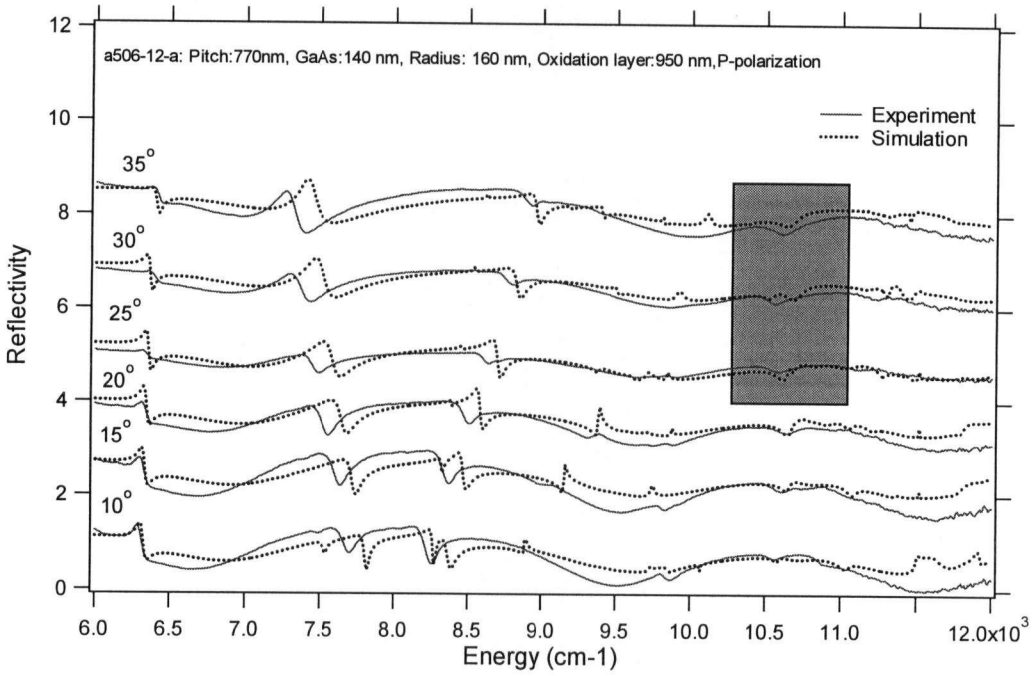

Figure 4.2: P-Polarization of experimental and simulated spectra for the Γ-X direction of the square lattice sample. The spectra are for incident angles of 10^0, 15^0, 20^0, 25^0, 30^0, and 35^0 from the bottom up. Solid lines represent experiment data; dashed lines represent simulation data. For clarity the curves have been offset vertically. The shaded region highlights where the out-going harmonic might be expected to resonant with leaky photonic eigenstates.

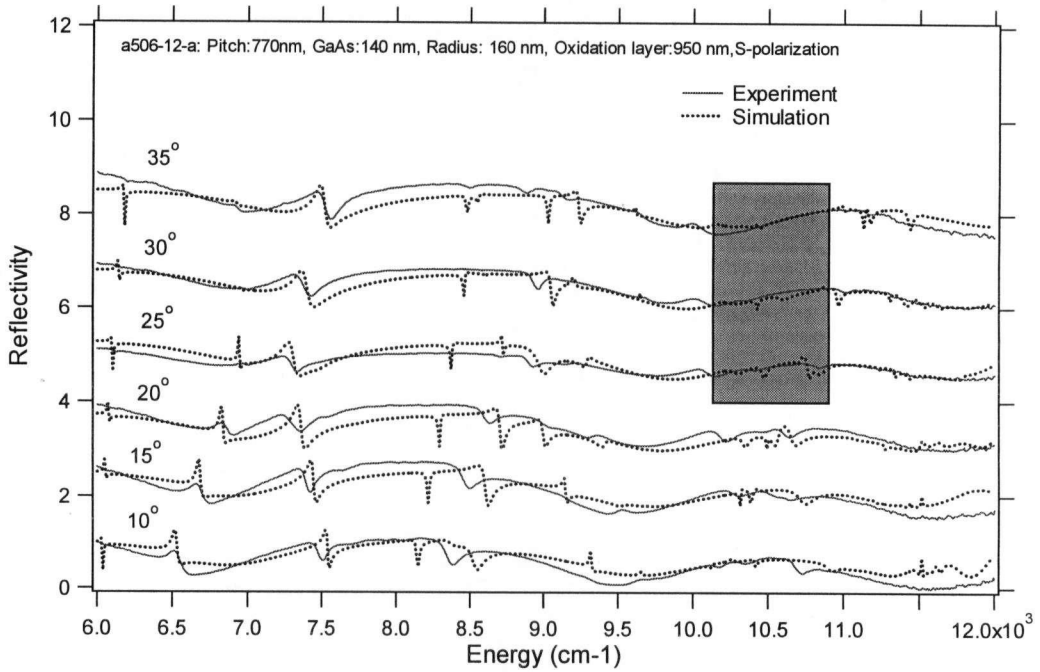

Figure 4.3: S-Polarization of experimental and simulated spectra for the Γ-X direction of the square lattice sample. The spectra are for incident angles of 10^0, 15^0, 20^0, 25^0, 30^0, and 35^0 from the bottom up. Solid lines represent experiment data; dashed lines represent simulation data. For clarity the curves have been offset vertically. The shaded region is the same as in Figure 4.2.

From figures 4.2 and 4.3 it is possible to qualitatively assess the band structure of this square lattice photonic crystal. It is well established [1,2,3,24] that in the limit of thin core layers, the four lowest order bands near zone center disperse away from the Γ point of the Brillouin zone in a well-defined pattern, three of them s-polarized, and the fourth p-polarized (see discussion in Chapter 2). The p-polarized band and one of the s polarized bands exhibit very weak dispersion, while the two remaining s-polarized bands disperse relatively strongly, one up and the other down in energy. The two weakly dispersive bands occur between 6,000 cm^{-1} and 6,400 cm^{-1} in Figures 4.2 and .4.3, and the upward dispersing s-polarized band appears in Fig. 4.3, starting at ~ 6,500 cm^{-1} at 10°, increasing to ~ 7,000 cm^{-1} at 25°. The lowest energy, downward dispersing s-polarized leaky band is not observed experimentally, as it occurs below the detector cutoff energy of ~ 6,000 cm^{-1}. This lowest energy band is, however, crucial for the second harmonic experiments, because it is the band that can be resonantly excited at the fundamental frequency corresponding to a wavelength of ~ 2 μm. Thus we have to rely on the model alone to estimate the dispersion of the band designed to resonant with the fundamental (in-coming) excitation laser in the second harmonic experiments.

The shaded regions in Figure 4.2 and Figure 4.3 shows where the second harmonic might possibly excite one of the higher lying bands; the out-going resonant process. In the p-polarized case, there is a very obvious, relatively flat band near 10,500 cm^{-1} that appears in both the experiment and the simulations. The flatness of this band offers the advantage of being able to fix the fundamental excitation spectrum from the optical parametric oscillator and the bandpass of the detection system (both described below) to a well-defined, and relatively narrow range of energies, independent of the incident angle. For this to work, the downward dispersing s-polarized band must exist at energies roughly half of this flat p-polarized band, or ~ 5,000

cm^{-1}. The situation for the s-polarized bands at high energy is slightly less clear. Close inspection indicates that there is in fact weak evidence of a low-energy, weakly dispersing mode in both the experiment and the simulations in this shaded region. There is also a more obvious upward dispersing s-polarized band in the experiment, at the high energy side of this shaded region. The experimental and simulated dispersion of the relevant bands, extracted from a detailed analysis of Figure 4.2 and Figure 4.3 for both s and p polarizations are shown in Figure 4.4. Because the lowest s-polarized band can not be measured by the detector, only the simulation curve is shown here. The inset shows that in the simulation, two p-polarized bands actually repel each other in the frequency range of interest,. The experimentally observed flat band is actually composed of the 'flat' potions of these two distinct p-polarized bands.

The solid curves and the dashed curves are the simulated and experimental results, respectively. Note that no obvious mode can be found in the experiment at 35° on the lowest of the high-energy set of dispersion curves, thus there are only four points on that particular curve.

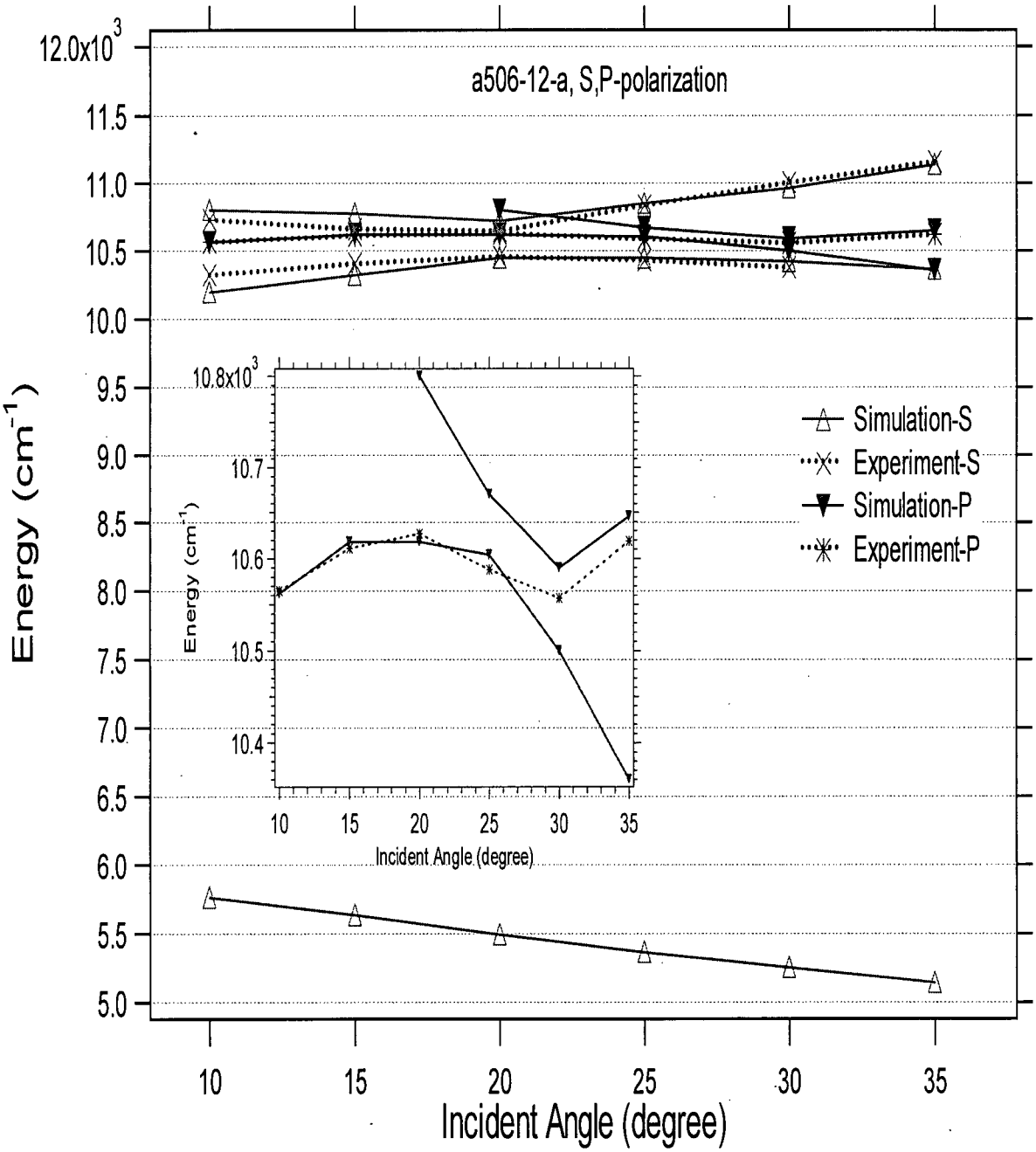

Figure 4.4: Dispersion curves of experimental and simulated results for s and p polarizations of the photonic crystal used in the nonlinear measurements described below. Just the lowest band, and the three higher bands relevant to the second harmonic predication are shown here. The lowest s dispersion curve can not be measured by the detector, so just the simulation curve is shown here. The solid curves and the dashed curves are the simulated and experimental results, respectively. Note here, no mode can be found in the experiment at 35° on the lowest of the high-energy set of bands. The inset shows that the flat p band observed experimentally seems to be made up of the flat parts of two simulation p bands that repel each other.

The solid curves and the dashed curves are the simulated and experimental results, respectively. Note that no obvious mode can be found in the experiment at 35° on the lowest of the high-energy set of dispersion curves, thus there are only four points on that particular curve.

It is clear from this plot that this sample is ideal for studying the resonant second harmonic conversion process. The downward s-polarized band is predicted by the simulations to span the half-energy of the flat p-polarized band corresponding to incident angles of the fundamental between 20 and 35 degrees. To clarify the relationship of these curves to the second harmonic experiment, Figure 4.5 shows the fundamental band dispersion at full scale, superimposed on the higher order bands plotted at half their frequency and in-plane wave vector.

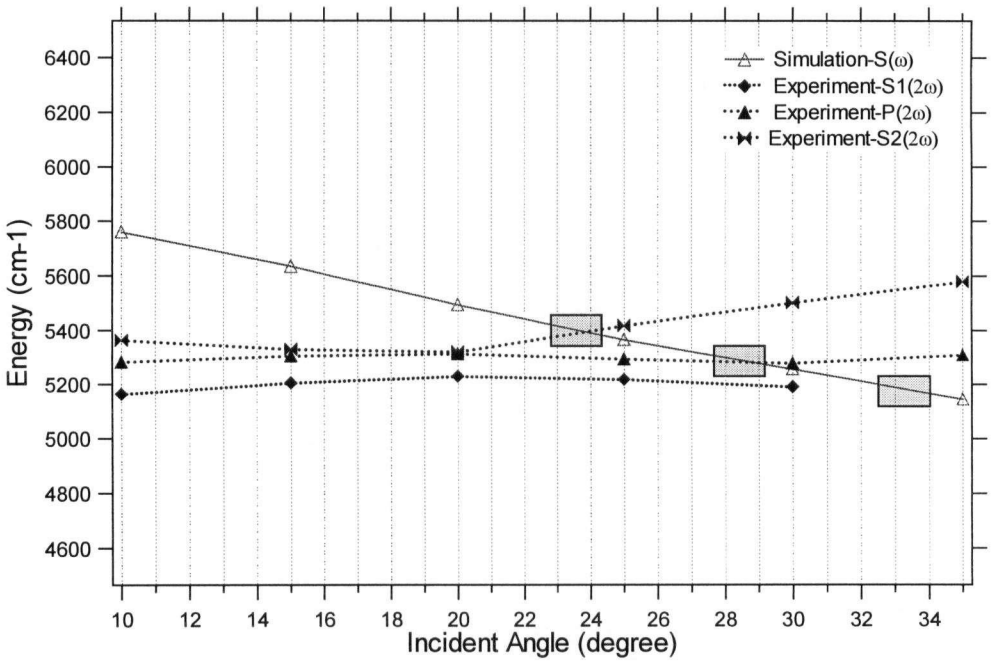

Figure 4.5: An enlarged depiction of the band structure over which the second-harmonic enhancement is expected to occur. The solid curve is the low frequency s-polarized band in Figure 4.3; the incoming resonance. The dotted curves are the experimentally measured high-frequency p- and s-polarized bands, which are plotted at half their frequency and in-plane momentum, respectively. The rectangles indicate the energy-incident angle windows where one might expect to see evidence of the double-resonant processes.

For incident light oriented along the Γ-X axis of the photonic crystal, the solid curve in Figure 4.5 represents the lowest s polarized band with which the fundamental field can be

resonant. The dotted curves represents the (scaled) dispersion of bands that can be resonant with the second harmonic polarization driven by the fundamental field with frequency and in-plane wave vector given by the scale values on the axes. If the fundamental falls on the solid curve only, there should be a resonantly enhanced second order polarization excited via the leaky photonic crystal mode (enhanced in comparison to the case in which the fundamental is not coincident with any curve in the figure), but the out-coupling of this enhanced second order polarization would not be influenced by the photonic bandstructure. If the fundamental frequency and in-plane wave vector fall on a dotted curve in Figure 4.5 the strength of the second order polarization driven by the unenhanced fundamental field will be similar to that which would be excited in the absence of any texture, but the out-coupling of the second order radiation to the top half-space will be influenced by the (higher order) bandstructure of the crystal. The doubly resonant SHG process will occur when the excitation conditions coincide with the crossing of one of the dotted curves with the solid curve. This double resonant condition results in a fully mode-matched nonlinear conversion process, effectively allowed in this periodic geometry by Bloch's theorem. From the linear dispersion data in Figure 4.5, the doubly resonant s-in p-out second harmonic conversion should occur when the incident fundamental frequency is ~5280 cm^{-1} (or a wavelength of ~1893 nm) at an incident angle of ~29° along the Γ-X direction. The corresponding second harmonic signal should occur near 10560 cm^{-1} (or a wavelength of 947 nm). Recall that these predictions are based on the simulated dispersion for the incoming resonance, which has not been directly measured using linear scattering spectroscopy. The precise positions of the double resonances are expected to differ slightly from those in Fig. 4.5, corresponding to a shift in the true incoming dispersion curve.

From this linear analysis we conclude that the fabricated sample achieved the design objectives outlined in chapter 2. In particular, the fundamental and second harmonic fields at the double resonant condition should both be well below the the GaAs band gap of 1.42 ev (11500 cm^{-1}), so there should be no complications introduced by linear absorption processes.

4.2 Second harmonic results

The experiment part of the second harmonic enhancement measurement was implemented by J. Mondia, at the University of Toronto. To observe these resonance enhancement effects, an optical parametric amplifier was used to produce ~200 fs long fundamental pulses at a repetition rate of 250 kHz in the range 1.5-2.0 μm. These pulses were incident on the photonic crystal membrane along the Γ-X direction from above. The spot diameter on the crystal was ~30 μm, and the incident angle was variable. The second harmonic signal was recorded using a liquid nitrogen cooled InGaAs detector. The second harmonic measurement was implemented according to the predication of the linear experiment and simulation.

The measured second harmonic spectra for an s-polarized input beam and both s-polarized and p-polarized second harmonic are shown for a range of incident angles in Figure 4.6 and Figure 4.7, respectively. An obvious intensity peak in the p-polarization occurs near 27°: there is a 60 fold difference between the peak intensities at 27° and 35°. For the s-polarization, the peak intensities do not change as much as in the p-polarized case, and the maximum intensity of the SHG in s polarization is 4 times weaker than the highest intensity of SHG in p polarization. Figure 4.8 and Figure 4.9 show the corresponding SHG simulation results for s polarization and p polarization, respectively, obtained using the non-linear code described in

chapter 2. The parameters for the non-linear code used in our simulation are listed in table 4.2. From the simulation results, the obvious intensity peak in the p-polarization can be seen at ~31° at an energy of 10,500 cm^{-1}.

Table 4.2: Simulation parameters used in non-linear code simulation

Parameter	Value
Pitch	770 nm
Hole Radius	160 nm
Core Thickness	140 nm
Oxide Thickness	950 nm
Hole Depth	140 nm
Resolution	0.7 cm^{-1}

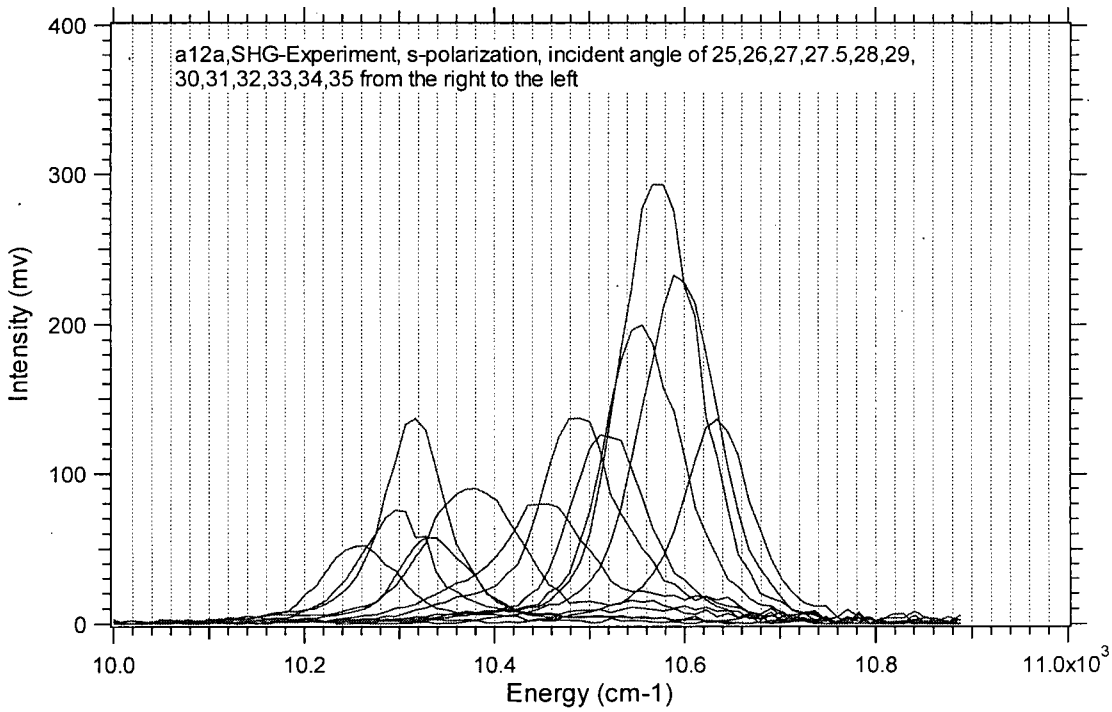

Figure 4.6: The experimentally measured SHG for s-in s-out polarization. From the right to the left, the measured incident angles range in single degree increments from 25 to 35 degrees. These spectra are normalized to the background second harmonic signal measured away from the patterned region of the sample.

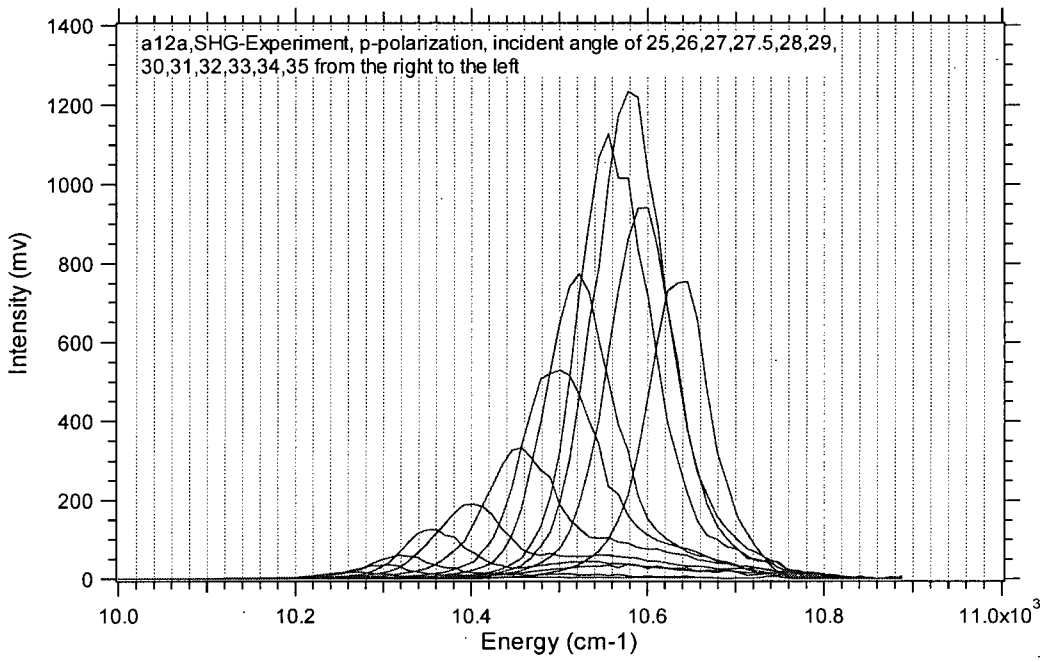

Figure 4.7: The experimentally measured SHG for s-in p-out polarization. From the right to the left, the measured incident angles ranging in single degree increments from 25, to 35 degrees. The spectra are normalized to the background second harmonic signal measured away from the patterned region of the sample.

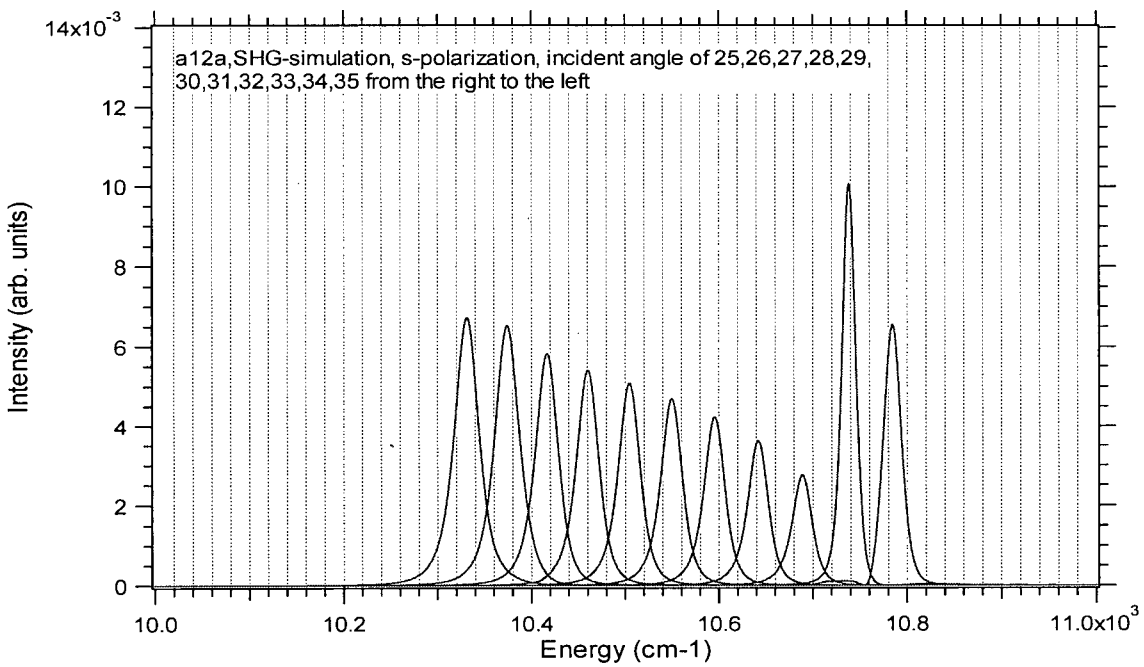

Figure 4.8: The simulated SHG results for s-in s-out polarization. From the right to the left, the measured angles increase in single degree increments from 25 to 35 degrees.

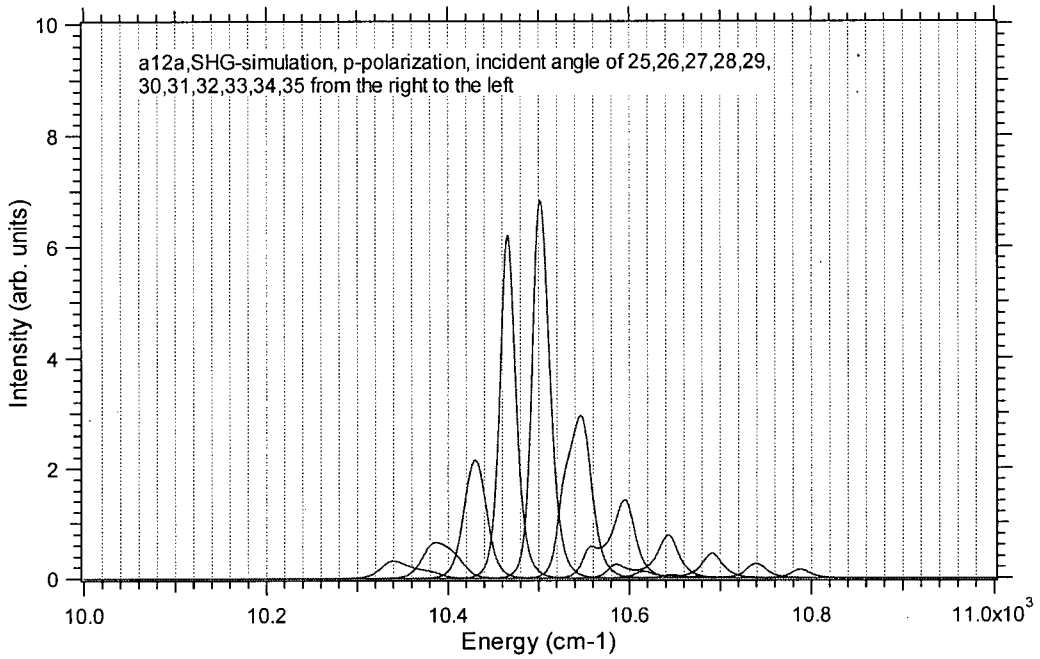

Figure 4.9: The simulated SHG results for s-in p-out polarization. From the right to the left, the angles increase in single degree increments from 25 to 35 degrees.

Figures 4.10 and 4.11 show corresponding contour plots of the experimental s-in p-out and s-in s-out SHG signal strengths respectively. Overall, the similarity of the simulated and measured results is remarkable given that the calculation is done for plane waves with well-defined in-plane wavevectors, and that the out-going resonant bands are of very high order (~ 12^{th} from the simulations). The dominant dispersive feature in both s and p polarized data sets is identical, and therefore it is assigned to the in-coming resonance. It also agrees with the simulated dispersion of the lowest s-polarized band to within < 1.3% (18meV) from 25 degrees to 35 degrees. Recall that this band is not directly detected in the linear dispersion measurements: the simulation that gives this level of agreement is based solely on the structural parameters of the crystal used to fit the higher lying bands. From this observation, we can take the dominant dispersion observed in the two second harmonic results as the dispersion of the

lowest s-polarized band in the sample. Figure 4.12 then shows all of the measured bands; the high-order, out-going bands obtained from the linear scattering data (at half their true energies), and the lowest s-polarized band from the SHG results (both s-in s-out and s-in p-out).

From Figure 4.12 one would therefore expect to observe the double resonant condition occur at an energy of ~ 10,600 cm^{-1} and an incident angle of 26 degrees for the s-in p-out polarization case, in excellent agreement with the peak in the p-polarized SHG contour plot (Figure 10). The predicted coordinates of the s-in s-out double resonance from Figure 4.12 are 10,400 cm^{-1} and 31 degrees. These coordinates actually correspond to the *minimum* in the corresponding SHG contour plot (Figure 11). This someone surprising result is discussed in more detail below.

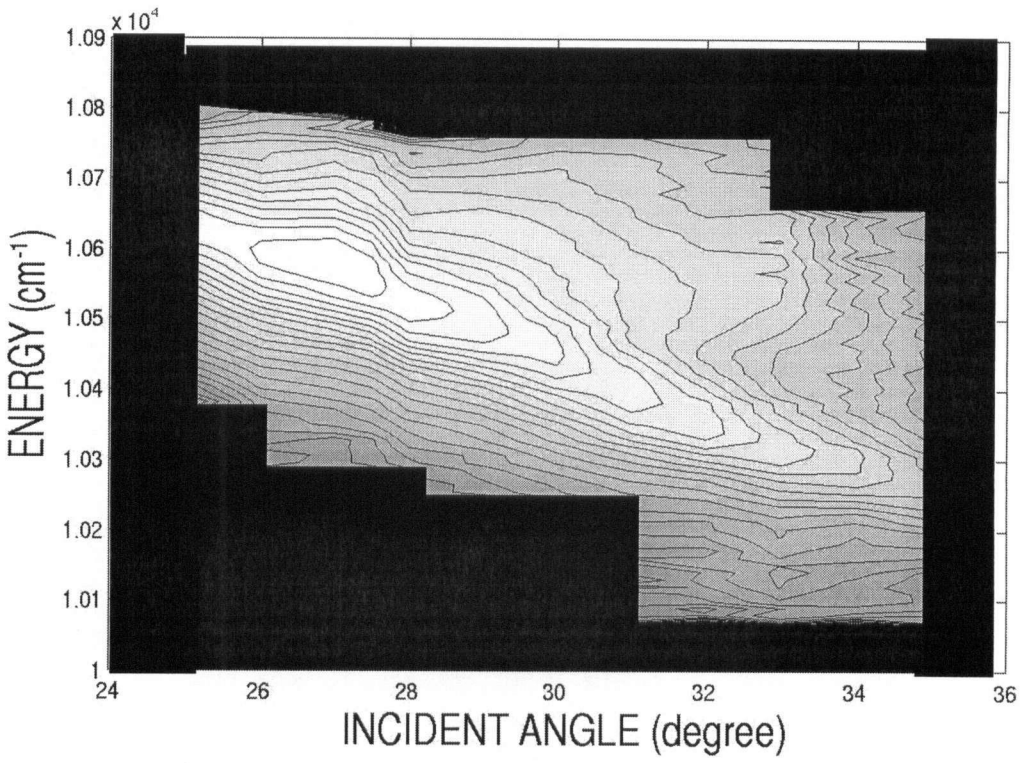

Figure 4.10: Measured relative second harmonic enhancement (on a logarithmic scale) as a function of the incident angle for s-in and p-out polarized beams. The distinct peak at around 27 degrees is direct evidence of the "double resonance" condition.

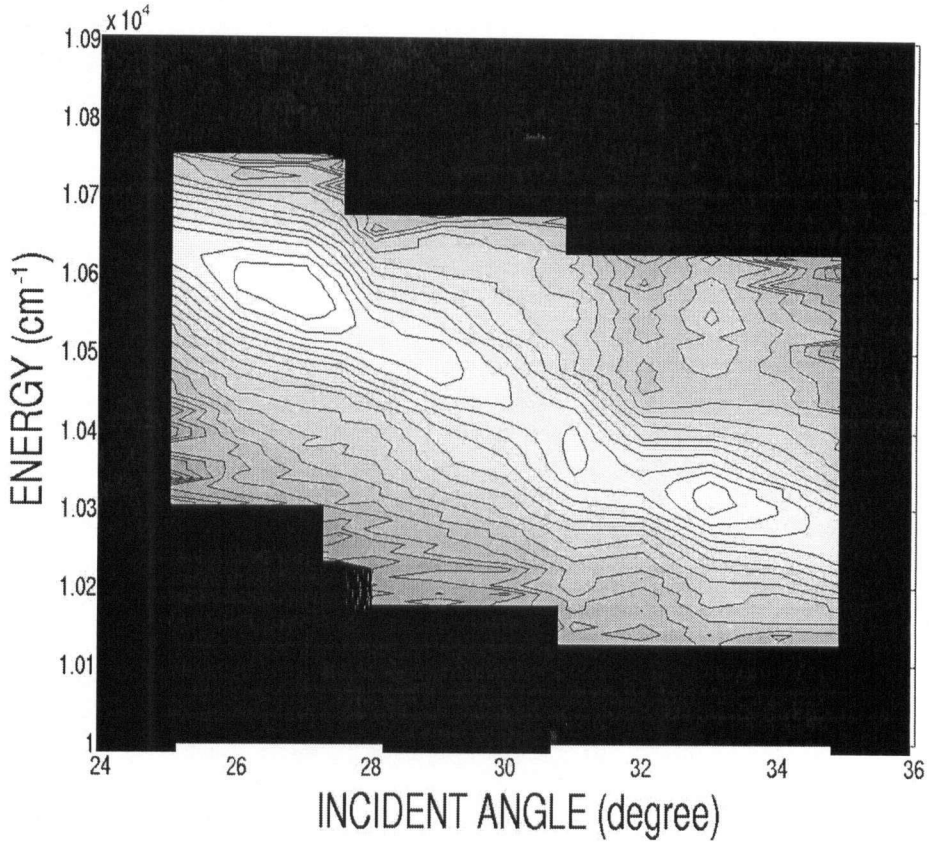

Figure 4.11: Measured relative second harmonic enhancement (on a logarithmic scale) as a function of the incident angle for s-in and s-out polarized beams.

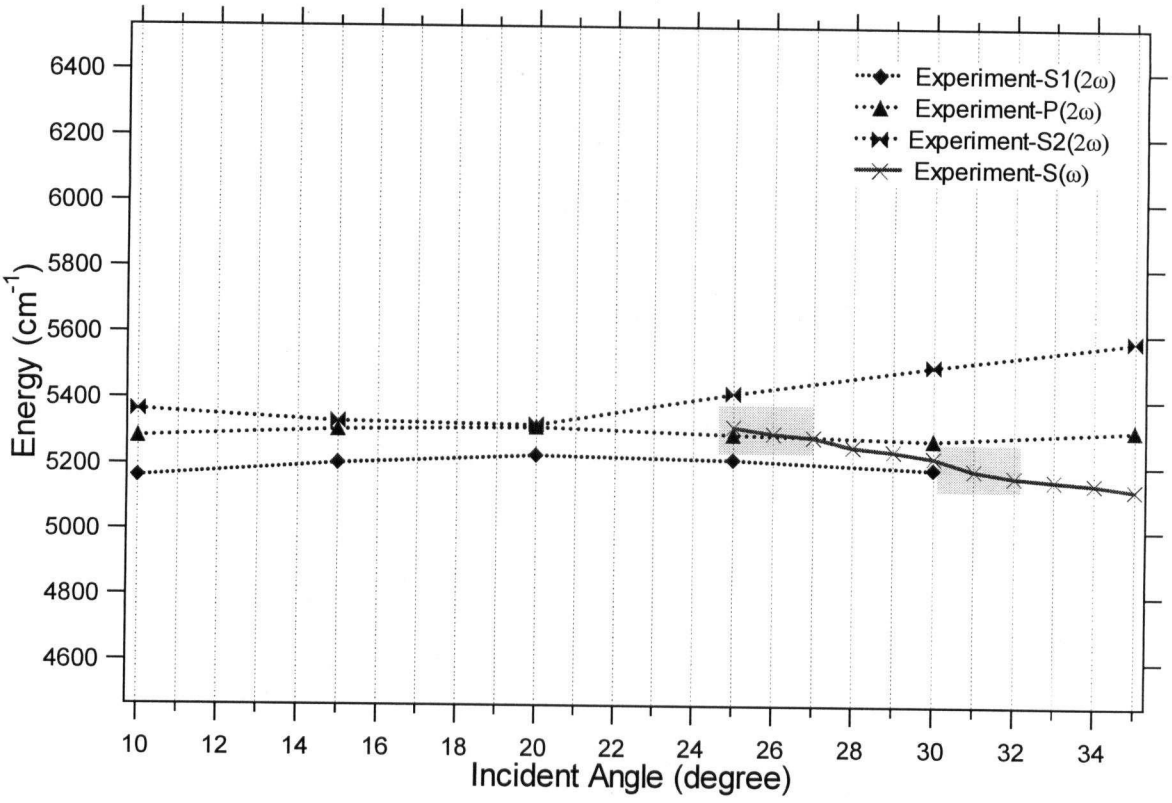

Figure 4.12: A depiction of the band structure over which the second-harmonic enhancement is to occur. It's a slightly revised version of Figure 4.5. The solid curve is the lowest s-polarized band from the experiment SHG results (both s-in s-out and s-in p-out). The dotted curves are the experimentally measured high-frequency p- and s-polarized bands, which are plotted at half their frequency and in-plane momentum, respectively. The rectangles indicate the energy-incident angle windows where one expects to see evidence of the double-resonant processes.

From the simulations, the width of the peaks ranges from ~20 cm^{-1} to ~40 cm^{-1}, while from the experiment, the width of the peaks ranges from ~80 cm^{-1} to ~100 cm^{-1}. The experimental linewidths are thus 2 times to 5 times broader than those calculated. At least part of this is expected, because the finite size of the incident optical beam represents a field with a range of in-plane wavevectors, while the simulation assumes excitation at a well-defined in-plane wavevector. In our second harmonic experiment, the spot size is approximately 30 μm. Based on simulations over an associated range of incident wavevectors around the centre wavevector, the broadening due to the finite beam size is approximately 60 cm^{-1}, consistent with the experimental results. The experiment therefore seems to effectively average the theoretical results over a range of incident angles.

The magnitude of the conversion efficiency has not yet been measured in an absolute sense. The ratio of the peak s-in p-out to s-in s-out enhancement predicted from the simulations over this range of phase space is ~1000. The measured ratio is 6. A lower limit on the resonant to off-resonant enhancement can be made by comparing the peak signal with that obtained at the same angle of incidence, but far off the resonant condition. For the p-out and s-out polarized data sets, the corresponding minimum enhancement factors are 1200 and 50 respectively.

The out-going resonance dispersions predicted in the simulations are considerably weaker than the in-coming resonance. This, combined with the broadening of the experimental results, makes it very difficult to quantify the out-going resonance from the measured data. In order to extract some information about the out-going resonance, attempts were made to fit the experimental data using a superposition of two –Gaussian peaks. Attempts were also made to fit the simulated SHG spectra with a double Gaussian function.

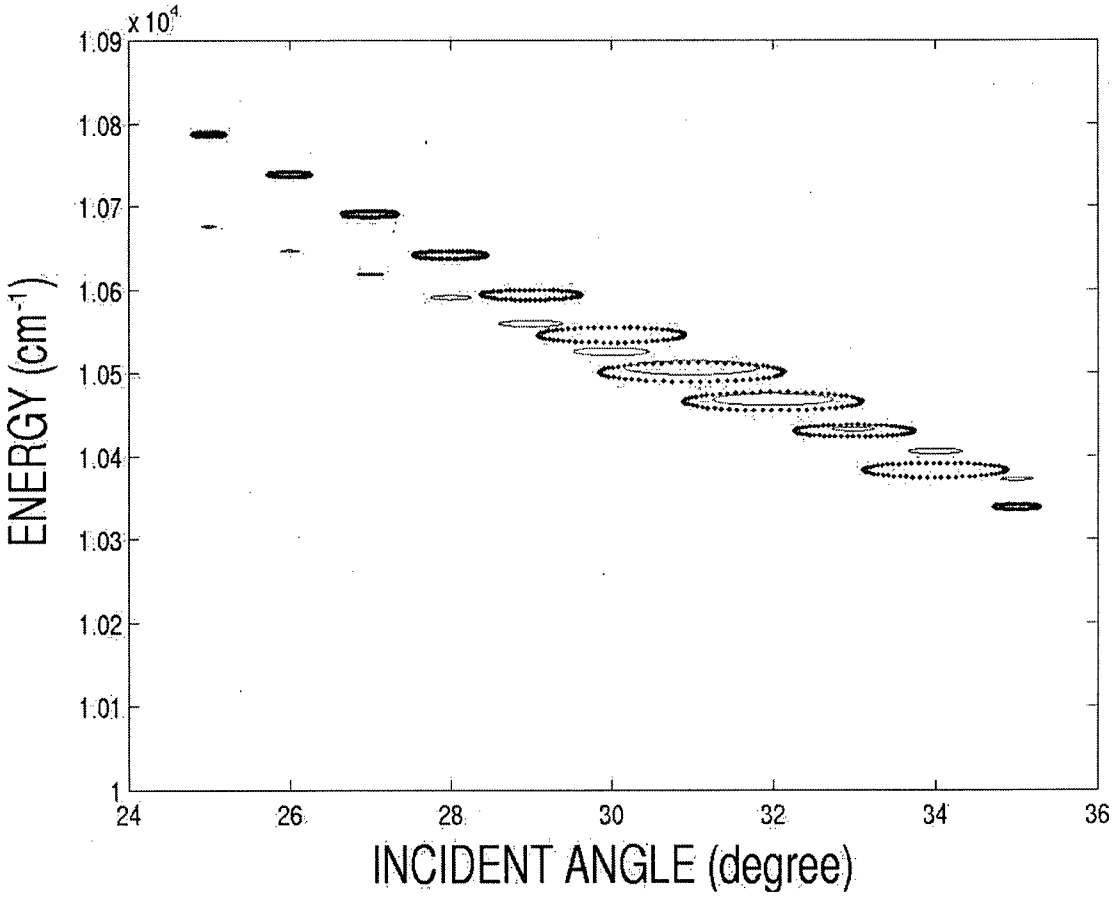

Figure 4.13: The simulation results for s-in p-out second harmonic generation based on two-Gaussian fits to the simulated second harmonic spectra. The dashed ellipses are centered on the incoming resonance, and the solid ellipses are centered on the outgoing resonance. The ellipse area represents the relative intensity of the Gaussian peaks. The linear dimensions of the ellipses imply nothing about the Gaussian linewidths.

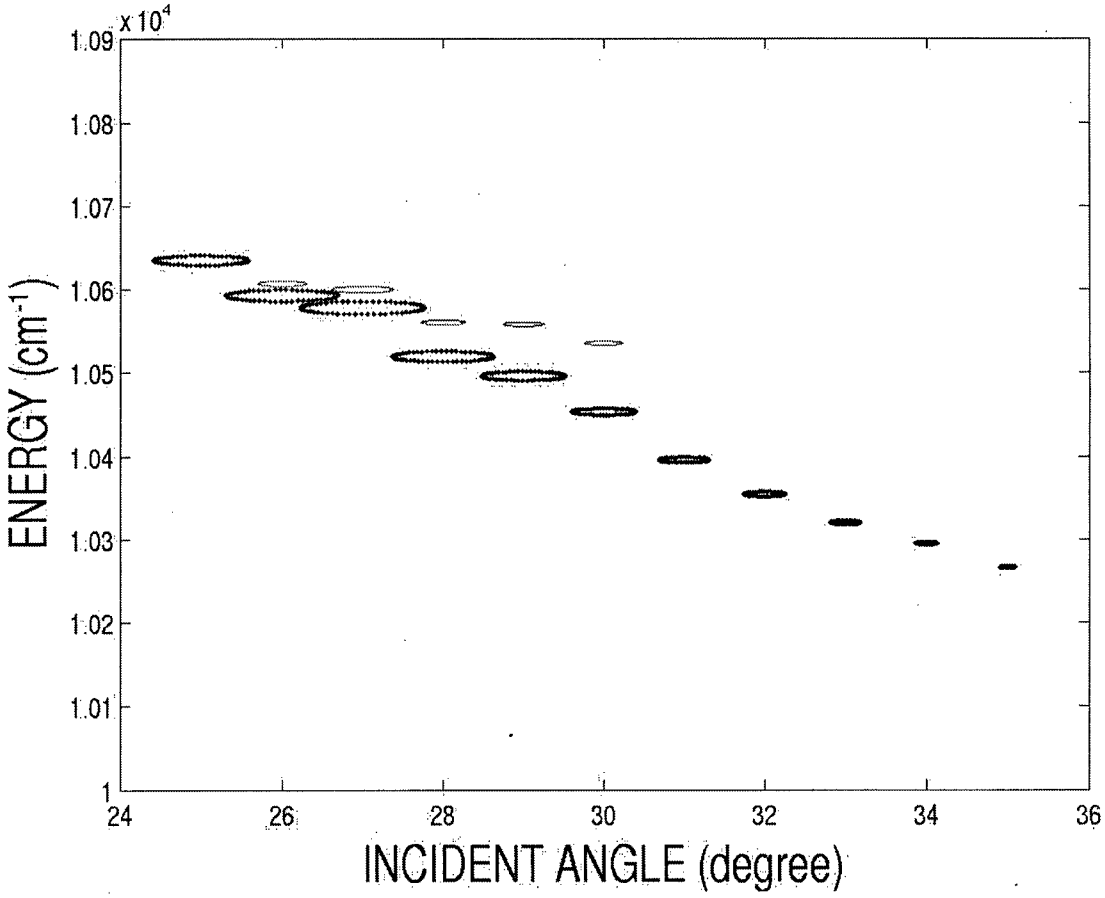

Figure 4.14: The experiment results for s-in p-out second harmonic generation based on two-Gaussian fits to the experimental second harmonic spectra. The dashed ellipses are centered on the incoming resonance, and the solid ellipses are centered on the outgoing resonance. The ellipse area represents the relative intensity of the Gaussian peaks.

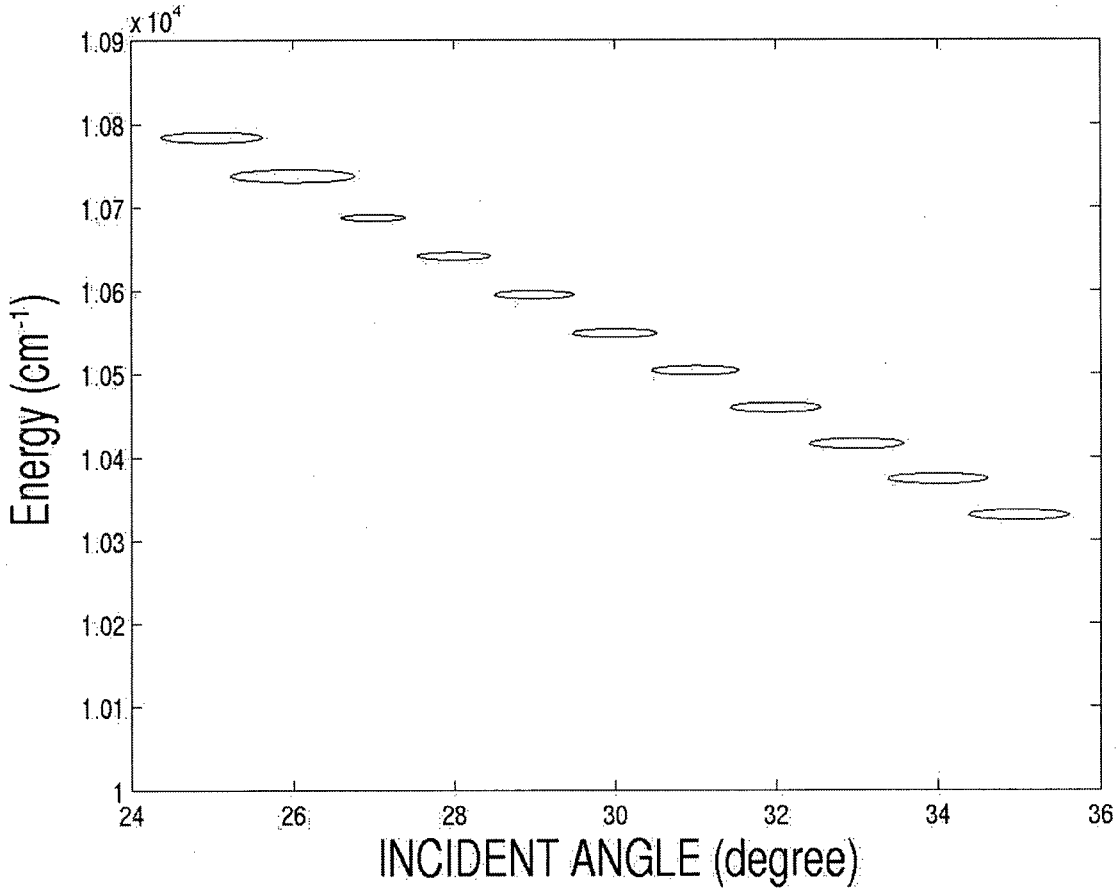

Figure 4.15: The simulation results for s-in s-out second harmonic generation based on an attempted two-Gaussian fits to the simulated second harmonic spectra. The solid ellipses are centered on the incoming resonance. There is no second harmonic from the outgoing resonance (only a single Gaussian could be fit to the data). The ellipse area represents the relative intensity of the peak 2nd harmonic signal. The linear dimensions of the ellipses imply nothing about the Gaussian linewidths.

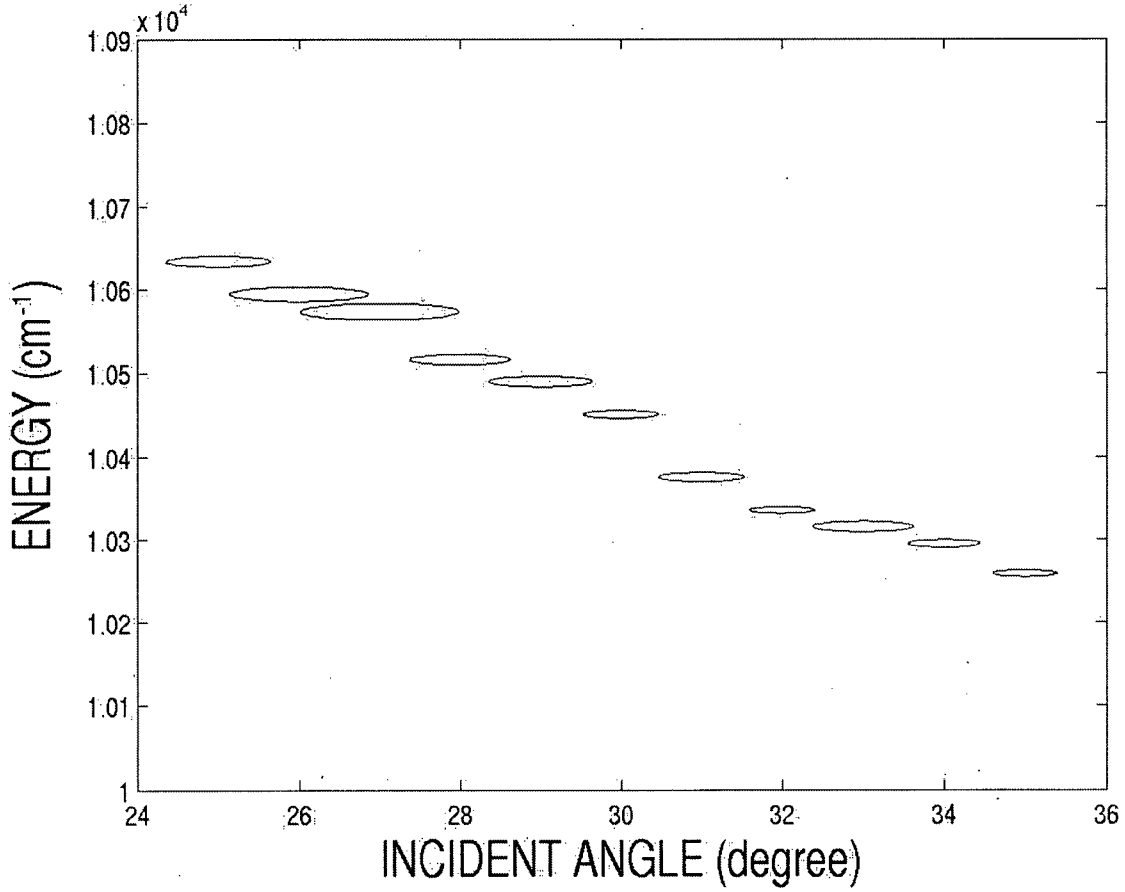

Figure 4.16: The experiment results for s-in s-out second harmonic generation based on an attempted two-Gaussian fits to the simulated second harmonic spectra. The solid ellipses are centered on the incoming resonance. There is no second harmonic from the outgoing resonance (only a single Gaussian could be fit to the data). The ellipse area represents the relative intensity of the peak 2nd harmonic signal.

For both theory and experiment, the s- in p-out spectra were easily fit using two Gaussian peaks, but the s-in s-out spectra were better described by a single Gaussian. For s-in p-out fits of the experiment results, the width of the outgoing peaks are at least 5 times wider than the width of the incoming peaks. The fits of the s-in p-out simulation results yielded outgoing peaks that are generally less than 2 times wider than the width of the incoming peaks. The p- polarized second harmonic signals generated using an s- polarized fundamental are shown in Figure 4.13

(simulation) and Figure 4.14 (experiment) at a variety of incident angles. The dashed ellipses are centered on the incoming resonance, and the solid ellipses are centered on the outgoing resonance. The ellipse area represents the relative intensity of the 2nd harmonic signal associated with the fitted Gaussian peaks. These plots were used to get the experimental in-coming dispersion shown in Figure 4.12.

The s-in s-out SHG for both simulation and experiment are shown in Figure 4.15 and Figure 4.16. In comparison to the s-in p-out polarized results, it was not possible to obtain good fits with a second Gaussian. Thus the s-in s-out results are unusual both with respect to the absence of a second peak (evidence of an outgoing enhancement), and in the double resonance condition occurring at a minimum in the SHG signal, as noted above.

To interpret all of these "expected" and "unexpected" results, the simulated SHG spectra are shown in Figures 4.17 to 4.20 for a range of incident angles, all superimposed on the corresponding in-coming and out-going linear reflectivity simulations. Figure 4.17 shows the s-in p-out SHG (solid) superimposed on the linear reflectivity simulations for s-polarized incident light at half the plotted frequencies (dash-dotted). The various curves correspond to incident angles from 25-35 degrees from the bottom to the top. All curves are shifted vertically to facilitate the comparison. The principal SHG peak in Figure 4.19 is therefore associated directly with the in-coming s-polarized band. There is no feature in the in-coming linear spectra associated with the secondary SHG peak on the shoulder of the main peak in the SHG spectra. However, Figure 4.18 shows the same SHG spectra superimposed on the p-polarized linear reflectivity spectra plotted on their natural frequency scale. The weaker peak in the SHG is clearly associated with this p-polarized out-going resonant mode, and the peak intensity in the SHG occurs when the in-coming and out-going resonances overlap. There are in fact several p-

polarized bands contributing to out-going enhancements here, but there is only one dominant mode. This basic behaviour is what one might naively expect based on the theoretical models described in chapter 2, and Figures 4.17 and 4.18 are fully consistent with the double resonant interpretation for the s-in p-out case discussed above.

Figure 4.19 and Figure 4.20 show the same comparison as in Figures 4.17 and 4.18, but for the s-in s-out polarization configuration. Again, from Figure 4.19 and Figure 4.20, the principal peak in the SHG is unambiguously associated with the incoming s-polarized mode. Interestingly though, the out-going s-polarized modes in almost all cases anti-resonate with the in-coming resonant process. In particular, the s-polarized out-going mode at ~ 10,400 cm^{-1} introduces a clear *reduction* in the net SHG throughout the whole range of angles where it overlaps with the relatively broad in-coming resonance. This observation explains the two "surprises" identified above when analyzing the s-in s-out SHG data. In particular, it is clear why it is impossible to fit two Gaussian *peaks* to what is clearly a Fano-like anti-resonant effect on the principal Gaussian-like in-coming resonance lineshape in the s-in s-out configuration. It is also consistent with the double resonant condition for the s-in s-out polarization case occurring at a *minimum* in the in-coming resonance curve.

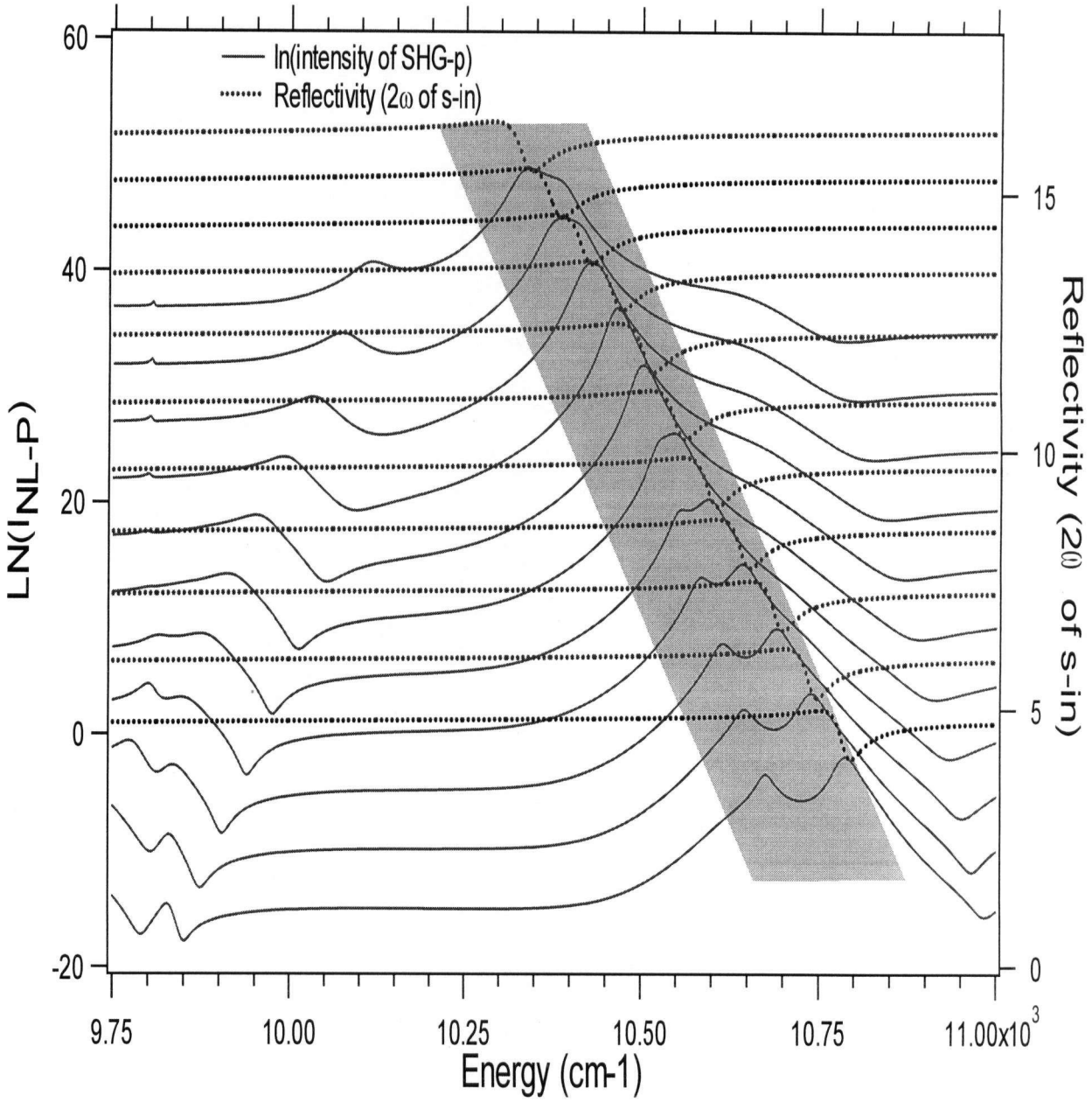

Figure 4.17: The relations between the second harmonic enhancement and the s-incoming polarization at 2ω. The curves correspond to incident angles ranging from 25 to 35 degrees from the bottom to the top. The solid curves represent the natural logarithm of the simulated SHG intensity. The dash-dotted curves show the simulated reflectivity of s-polarized light at half the indicated frequency (the incoming resonance). These curves are shifted to facilitate the comparison. The shaded region highlights the in-coming and out-going resonantly enhanced SHG peaks. Only the main peak in the SHG is associated with the in-coming s-polarized resonance, but this association is obvious.

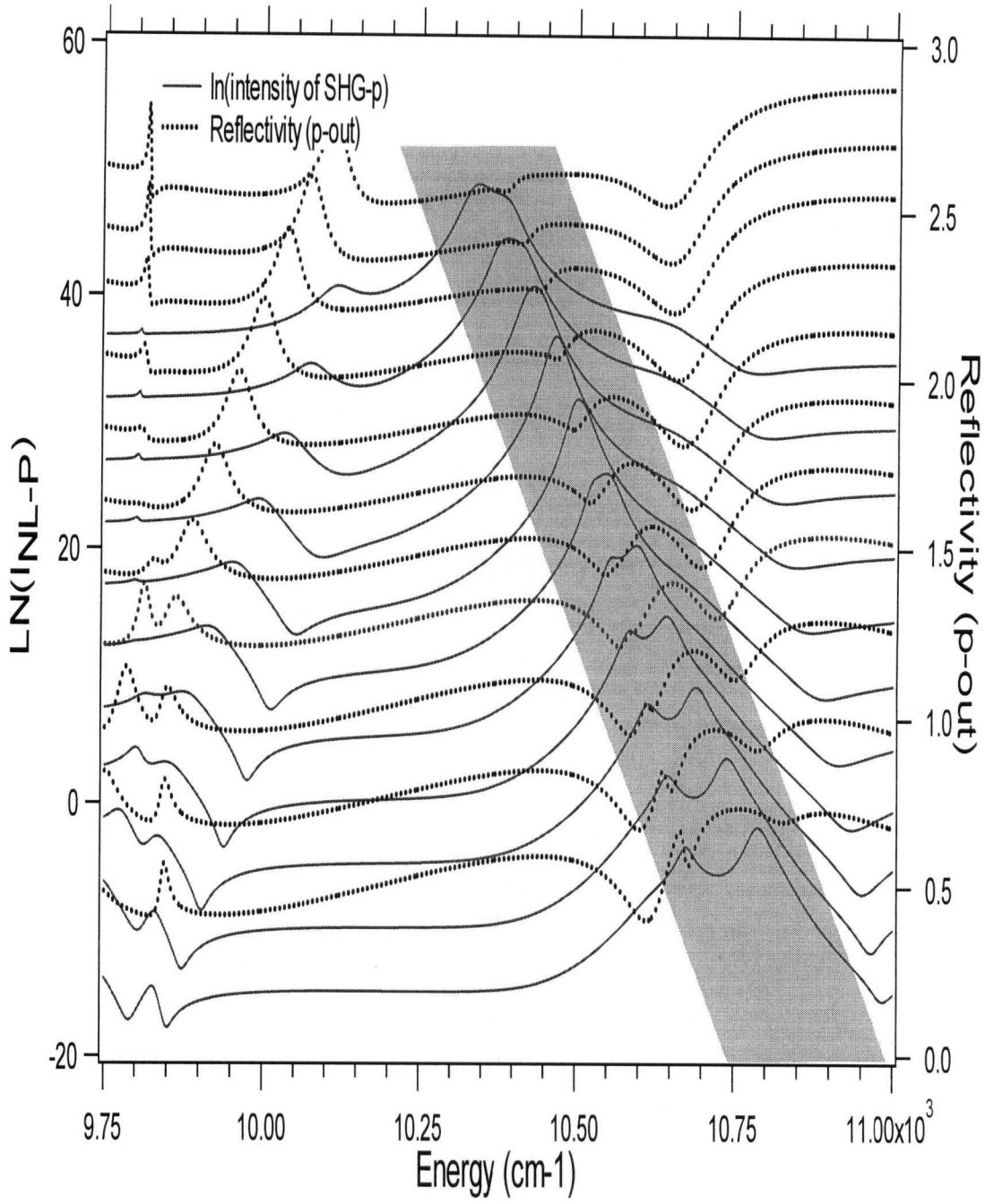

Figure 4.18: The relations between the second harmonic enhancement and the p-outgoing polarization. The curves correspond to incident angles ranging from 25 to 35 degrees from the bottom to the top. The solid curves represent the natural logarithm of the simulated SHG intensity. The dash-dotted curves show the simulated reflectivity of p-polarized light at the indicated frequencies. These curves are shifted to facilitate the comparison. The shaded region highlights the in-coming and out-going resonantly enhanced SHG peaks. Clearly the secondary peak in the SHG is associated with features in the p-polarized reflectivity spectrum, although there appears to be more than a single p-polarized mode involved in these simulated results.

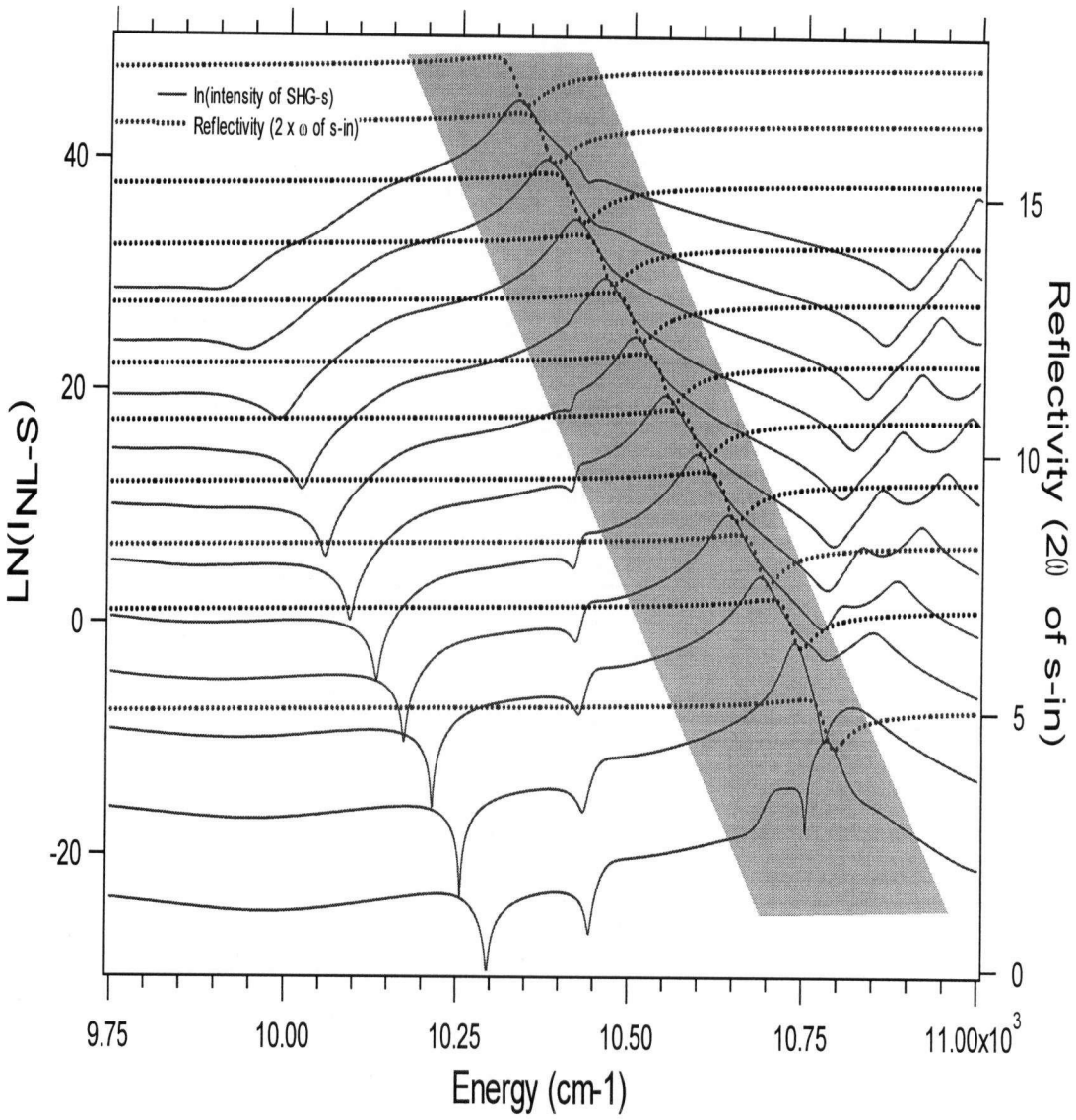

Figure 4.19: The relations between the second harmonic enhancement and the s-incoming polarization at 2ω. The curves are corresponded to 25, 26, 27, 28, 29, 30, 31, 32, 33, 34, and 35 incident angles, respectively. The solid curves represent the natural logarithm of intensity of the SHG. The dash-dotted curves show the reflectivity of s(ω)-in at 2 ω. These curves are shifted to facilitate the comparison. The clear trend can be seen that the SHG peak (shaded region) is due to the incoming s mode.

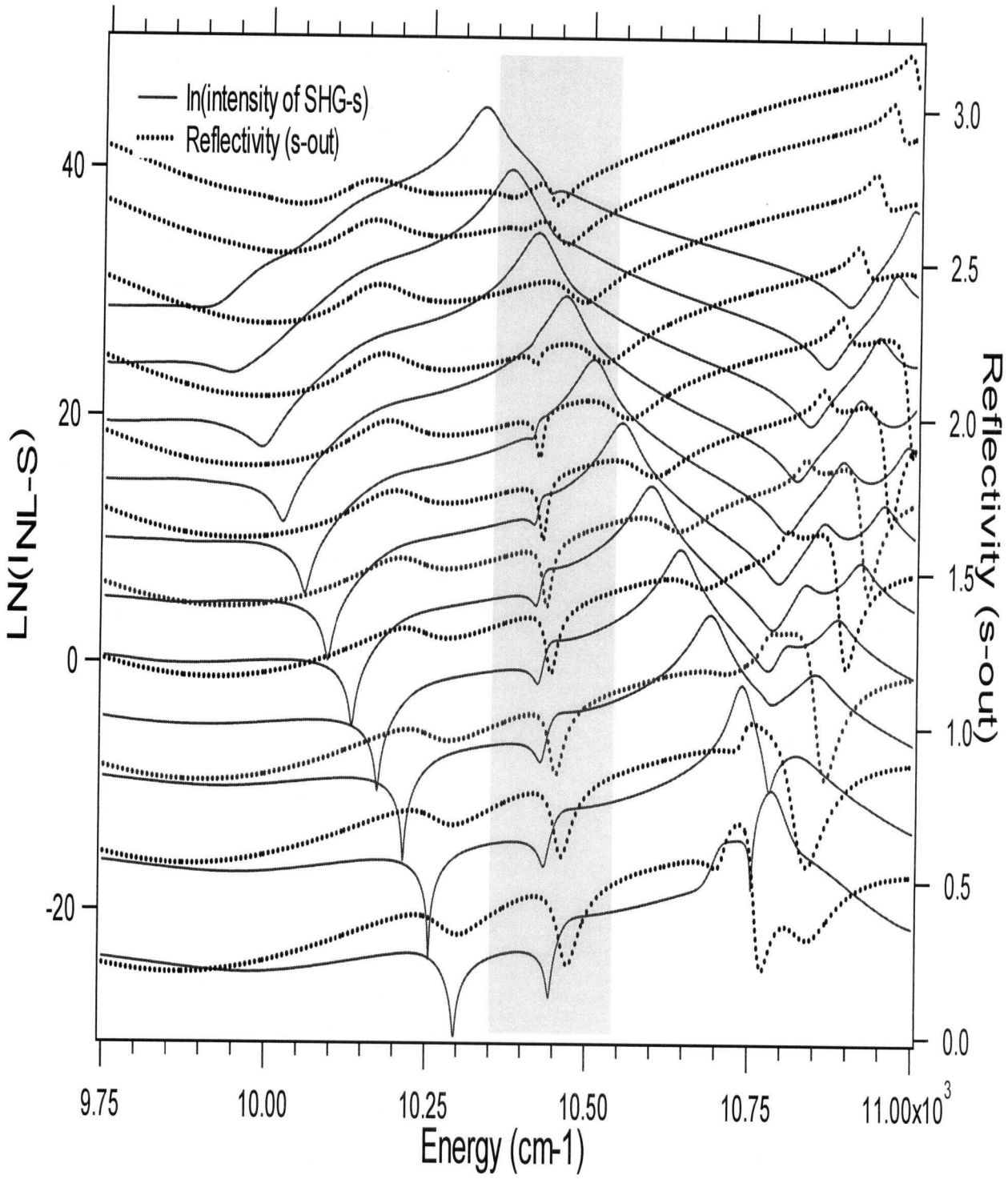

Figure 4.20: The relations between the second harmonic enhancement and the s-outgoing polarization. The curves are corresponded to 25, 26, 27, 28, 29, 30, 31, 32, 33, 34, and 35 incident angles, respectively. The solid curves represent the natural logarithm of intensity of the SHG. The dash-dotted curves show the reflectivity of s(ω)-in at 2 ω. These curves are shifted to facilitate the comparison. No clear trend can be seen that SHG peak is due to the outgoing s mode. The shaded region highlights the flat antiresonant effect of one of the outgoing s-polarized resonances.

Chapter 5

Conclusions

A square lattice of through-holes etched into a 140 nm thick layer of GaAs supported on a ~ 1μm thick alumina cladding layer was designed so that fundamental light at a wavelength of ~ 2μm could resonantly excite the lowest order band of leaky photonic eigenstates characteristic of the strongly textured membrane waveguide. The designed pitch of the lattice was 770 nm, and the hole diameter was 320 nm, These parameters were chosen so that the energy of the second harmonic, near 10,000 cm^{-1} would be less than the band gap energy of the GaAs at 11,400 cm^{-1} to avoid complications due to interband absorption. A sample was fabricated to these specifications using a series of processes that included, pre-cleaning and drying, spin coating ~ the sample with ~200 nm of a plastic resistant layer, e-beam lithography, developing, etching, and oxidation.

Linear specular reflectivity spectra of the sample were measured at a variety of incident angles using a white light source and a Bomem DA8 Fourier Transform Interferometer (FTIR) spectrometer. The physical parameters of the processed sample (GaAs layer thickness, hole size and pitch etc.) were determined to be close to the design specifications by curve-fitting the reflectivity spectra with simulation software. Based on these measured and simulated dispersion curves, it was predicted that strong second harmonic enhancement due to both in-coming and out-going resonances should be observable in this sample when the incident fundamental frequency is ~5280 cm^{-1} (or wavelength of ~1893 nm) at the incident light of 30° along the Γ-X direction of the photonic crystal. This puts the second harmonic near 10560 cm^{-1}, safely below the GaAs band gap.

The second harmonic signal reflected from the sample surface in the specular direction was measured at the University of Toronto by Jessica Mondia, using an optical parametric amplifier as a strong light source at the fundamental frequency of ~ 5000 cm^{-1}. The optical parametric amplifier generates 200 fs fundamental pulses at a repetition rate of 250 kHz in the range 1.5-2.0 μm. These pulses were incident on the photonic crystal membrane along the Γ-X direction for different incident angles based on the above stated predication. Non-linear simulation results were also used to compare with the non-linear experiment results.

Both model calculations and experimental results clearly demonstrate that the second harmonic conversion efficiency is dramatically enhanced when the fundamental field excites a low-energy s-polarized photonic band of the textured membrane waveguide structure. In the case of p-polarized second harmonic radiation, a peak enhancement of over ~1200 times is observed at the energy of a flat, high-energy band that is clearly evident in the linear p-polarized reflectivity spectra. For the s-in, p-out polarization configuration the conversion efficiency is a maximum at the "double-resonance" condition, which occurs at ~10,570 cm^{-1} nm at an incident angle of ~ 27°. This was what was expected based on nonlinear simulations and intuition. The unexpected result is that for the s-in s-out polarization configuration, the out-going resonance appears to add destructively to the in-coming resonance, resulting in a local minimum at the double resonance condition, rather than a local maximum.

Overall, the simulated and experimental results are in excellent qualitative agreement. The incoming resonance and the out-going resonances are shifted by less than 1.3% and 0.5% in energy respectively. The main discrepancy is the linewidth of the linear and nonlinear spectra, which are consistently broader in the experimental results. Much of this broadening is due to the

small spot sized used in the experiment, as compared to the plane wave excitation assumed in the model. Additional broadening is expected due to sample imperfections.

This work provides clear proof that 2D photonic crystals in GaAs membrane waveguides can be used to substantially enhance the nonlinear optical conversion of a fundamental field incident from the top half-space, to a field at twice the fundamental frequency propagating away in the specular direction. The enhancement occurs via a micro-cavity enhancement effect associated with the in-coming resonant excitation of leaky photonic eigenstates localized to the membrane. This generates large internal fields that drive a correspondingly enhanced nonlinear polarization at twice the fundamental frequency. When this second harmonic polarization is resonant with a high-lying photonic crystal band, the overall conversion can either be enhanced, or degraded, depending on the relative phase of the two resonant contributions. In the experiments reported here, the s-in, p-out polarization configuration led to an unambiguous overall enhancement. In the s-in, s-out polarization configuration there is also clear evidence of double-resonant effects, but the interpretation, at least based on the theoretical simulations, suggests that there is some anti-resonant coupling in this geometry.

These results illustrate one example of how 2D planar photonic crystals etched into semiconductor membranes can be used to engineering nonlinear optical phenomena. Numerous other nonlinear optical phenomena are expected to be tailorable using similar approaches to achieve specific objectives. There are many opportunities to extend this work to develop nonlinear optical engineering concepts in these structures. Obvious avenues for future work include using purely bound states rather than leaky states, and extending the fundamental nonlinearity to include frequency difference and higher order nonlinear effects.

Reference

[1] A.R. Cowan. Periodically textured planar waveguides. Master's thesis, University of British Columbia, 2000.

[2] A.R. Cowan, P. Paddon, V. Pacradouni, and Jeff F. Young. Resonant scattering and mode coupling in two-dimensional textured planar waveguides. Journal of the Optical Society of America, 18(5), 2001.

[3] W.J. Mandeville. Quantitative linear optical scattering spectroscopy of two-dimensionally textured planar waveguides. Ph.D.'s thesis, University of British Columbia, 2001.

[4] http://www.jcnabity.com

[5] J.C. Nabity. Nanometer pattern generation system, 2001.

[6] R.E. Sah, J.D. Ralston, S. Weisser, and K. Eisele. "Characteristics of a two-component chemically-assisted ion-beam etching technique for dry-etching of high-speed multiple quantum well laser mirrors". Applied Physics Letters, 67(7), 1995.

[7] F. Sfigakis. Optical characterization of $Al_xGa_{1-x}As$ oxides. Master's thesis, University of British Columbia, 1999.

[8] F. Sfigakis, P. Paddon, M. Adamcyk, C. Nicoll, A.R. Cowan, T. Tiedje, and Jeff F.Young. "Near-infrared refractive index of thick, laterally oxidized AlGaAs cladding layers". Journal of Lightwave Technology, 18(2):199{202), 2000.

[9] A.Fiore, V.Berger,E.Rosencher,P.Bravetti, and J.Nagle. "Phase matching using an isotropic nonlinear optical material". Nature, 391, 143,1998.

[10] J. E. Sipe, ''New Green-function formalism for surface optics,'' J. Opt. Soc. Am. B 4,481 (1987).

[11] E. Yablonovitch. "Inhibited spontaneous emission in sold state physics and electronics". Phys. Rev. Lett. 58:2059, 1987.

[12] S. John. "Strong localizaation of photonc in certain disordered dielectric superlattices". Phys. Rev. Lett. 58:2486, 1987.

[13] E. Yablonovitch, T.J. Gmitter, and K.M. Leung. "Photonic band structures: The face-centered cubic case employing non-spherical atoms". Phys. Rev. Lett. 67:2295, 1991.

[14] K. M. Ho, C.T. Chan and C.M.Soukoulis. "Exotence of a photonic bandgap in periodic dielectric structures', Phys. Rev. Lett.65:3125,1990.

[15] M.E. Zoorob, M.D.B. Charlton, G.J.Parker, J.J. Baumberg, and M.C. Netti. "Compelete and absolute photonic bandgaps in highly symmetric quasicrysatls embedded in low refractive index materials", Mat. Sci. Eng. B74(2000),168.

[16] J.G.Fleming and S.Y.lin, "Three-dimensional photonic crystal with a stop band from 1.35 to 1.95 μm", Opt. Lett. 24(1999), 49.

[17] V. Pacradouni, W. J. Mandeville, A. R. Cowan, P. Paddon, Jeff F. Young, and S.R.Johnson. "Photonic band structure of dielectric membranes periodically textured in two dimensions". Phys. Rev. B **62**(2000), 4204.

[18] M. Scalora, J. P. Dowling, C. M. Bowden and M. J. Bloemer. "Optical limiting and switching of ultrashort pulses in nonlinear photonic band gap materials", Phys. Rev.Lett. 73(1994), 1368.

[19] J.A. Armstrong, n. Bloembergen, J. Ducuing, and P. S. Pershan. "Interactions between light waves in a non-linear dielectrc", Phys. Rev. 127 (1962), 1918.

[20] V. Berger. "Nonlinear photonic crystals", Phys. Rev. Lett. 81(4136),1998.

[21] N. G. R. Broderick, G. W. Ross, H. L. Offerhaus, D.J. Richardson, and D. C. Hanna. "Hexagonally poled lithium niobate: a two-dimensional nonlinear photonic crystal", Phys. Rev. Lett. 84(2000), 4345.

[22] A.R. Cowan and Jeff F. Young. "Mode matching for second-harmonic generation in photonic crystal waveguides", Phys. Rev. B, 65(2002),085106-1.

[23] W.M.Robertson and G.Arjavalingam. "Measurement of photonic band structure in a two-dimensional periodic dielectric array", Phys. Rev. Lett. 68(1992),2023.

[24] P.Paddon and Jeff F. Young. "Two-dimensional vector-coupled-mode theory for textured planar waveguides", Phys. Rev. B. 61(2000),2090.

[25] R. D. Meade, K.D.Brommer, A.M.Rappe, and J.D. Joannopoulos. "Existence of a photonic band gap in two dimensions", Appl. Phys. Lett. 61(1992), 495.

[26] Jeong-Ki Hwang, Han-Youl Ryu, Dae-Sung Song, Il-Young Han, Hyun-Woo Song, Hong-Kyu Park, and Yong-Hee Lee. "Room-temperature triangular-lattice two-dimesional photonic band gap lasers operating at 1.54 μm", Appl. Phys. Lett. 76(2000), 2982.

[27] J. D. Joannopoulos, R. D. Meade, and J. N. Winn. "Photonic crystals: molding the flow of light", (Princeton University Press, New Jersey, 1995).

[28] S.Y.Lin,J.G.Fleming, D.L.Hetherington, B.K.Smith, R.Biswas, K. M. Ho, M. M. Sigalas, W. Zubrzycki, S.R.Kurtz, and J. Bur. "A three-dimensional photonic crystal operating at infrared wavelengths", Nature, 394(1998), 251.

[29] M. Campbell, D. N. Sharp, M.T.Harrison, R.G. Denning, and A. J. Turberfield. "Fabrication of photonic crystals for the visible spectrum by holographic lithography",

Nature, 404(2000), 53.

[30] In this thesis, the non-linear code I used was developed by a undergraduate student, Kuljit Singh Virk, in our lab.

[31] A. A. Busch. An electron beam lithography system: setup and characterization. Master's thesis, University of British Columbia, 1992.

[32] "DesignCAD 2-D Reference menual, Version 6", (American Small Business Computers,Inc.).

[33] N.W.Ashcroft, and N.D.Mermin."Solid State Physics", (Harcourt Brace Colledge Publishers, 1976).